Université de Sherbrooke

# The Application of Scanning Tunneling Microscopy (STM) and Related Techniques to the Study of Organic and Biomolecular Targets

by

Jing KANG

Département de Médecine Nucléaire et Radiobiologie

Master Thesis presented to Faculté de Médecine for obtaining the Master degree in Science (M. Sc.)

August 1996

# Table of materials

# Acknowledgment

I thank all the people who have helped me and wish to express my special gratitude to:

My supervisor Dr. Paul A. Rowntree who introduced me, as a physicist, to the 'golden' STM world. His stimulating instructions, constructive criticisms, passionate feeling for science, and sense of humor made this work enjoyable and worthwhile.

Dr. Kim D. Truong for her assistance in preparing and characterizing the butanethiol SAMs by IR-RAS and valuable discussions on science and life.

Caroline Olsen and Jean-François Picard for their friendship, collaboration in the work and for translating the abstract of the thesis into French.

Dr. Léon Sanche and his colleagues, Marc Michaud, Hongyue Shi, Martin Lepage, Pierre-Cyrille Dugal, Luc Parenteau and Daniel Robillard for providing the instrument and a friendly environment in preparing the gold samples.

The Medical Research Council and Natural Sciences and Engineering Research Council (Canada) for supporting this work.

My husband Rutao Yao and my son Benjamin-Tianjian Yao for providing me with the moral support and giving me so much pleasure throughout the whole work.

# List of Figures

# List of Abbreviations and symbols

ADC: Analog-to-Digital Converter

AFM: Atomic Force Microscopy

$C_n$: $CH_3(CH_2)_{n-1}SH$

DNA: Deoxyribonucleic acid

$E_F$: the Fermi Energy

*fcc*: face-centred cell

*hcp*: hexagonal close-packing

HOMO: Highest Occupied Molecular Orbital

HOPG: Highly Oriented Pyrolytic Graphite

IR-RAS: Infrared Reflection Adsorption Spectroscopy

LDOS: Local Density of States

LUMO: Lowest Unoccupied Molecular Orbital

MO: Molecular Orbital

***P***: Piranha acid

***S***: Sulfochromic acid

SAM: Self-Assembled Monolayer

SCG: Single Crystal Graphite

SPM: Scanning Probe Microscopy

STM: Scanning Tunneling Microscopy

TEM: Transmission Electron Microscopy

UHV: Ultra-High Vacuum

# Abstract

Scanning tunneling microscopy (STM) has been used to study: (a) Self-assembled monolayers and sub-monolayers of butanethiol adsorbed onto highly uniform Au/mica films, (b) DNA adsorbates on different substrates prepared by different deposition techniques. In addition, surface preparation techniques have been investigated. Two strongly oxidizing solutions ( sulfochromic and piranha acids) have been studied for the elimination of residual organic adsorbates on the Au/mica substrate. Treatment of the Au/mica surface with piranha acid leads to extensive and uncontrolled etching of the surface, and severe disruption of the surface topography. Limited exposure of the Au/mica surfaces to sulfochromic acid leads to the formation of permanent etch pits of the surface that are exclusively one Au layer deep; extended exposure leads to progressive lateral etching of the surface, ultimately leading to the formation of 3.3-3.6 Å high islands on the otherwise flat surface. This well-controlled sulfochromic acid etching procedure was used for the substrate preparation in subsequent experiments.

STM images taken of fully-equilibrated butanethiol monolayer films show molecularly resolved features that are believed to correspond to the methyl terminations of the organic surface. Large domains of organized adsorbates and a variant of the previously reported $p\times\sqrt{3}$ superlattice structure is observed on these surfaces; using this nomenclature, the basic repeat unit of the structure reported herein corresponds to a $7\times\sqrt{3}$ superlattice. Lateral variations in the elevations of striped structures are tentatively assigned to thiolates bound into non-equivalent sites ( i.e., *fcc* and *hcp* sites) of the Au(111) substrate. We have also observed molecular structure in regions of the superlattice that were structureless in UHV-STM studies. These observations suggest that the filling-factor of the fully equilibrated surfaces is highly sensitive to the manner of sample preparation and storage. The study of sub-monolayer films shows the island-like formations of SAMs on the gold surface; each island has same molecular structure as observed in monolayer films. Large-scale desorption

of thiolates does not appear to be a necessary step in the formation of highly organized films of the short-chain systems when equilibrated in thiol/methanol solutions, and the sample processing history may have significant effects on the ultimate surface topography.

Natural plasmids of different lengths together with chemically modified oligonucleotide sequences are adsorbed onto graphite and Au/mica surfaces and studied using the STM. High resolution images were obtained with clearly resolved helical structures; the structural dimentions are in good agreement with those B-form of DNA. This kind of molecular observation was very rare; even low resolution images could not be routinely obtained for natural plasmids. Surface modification and molecular combing techniques were also applied; the deposition of the biological adsorbates is clearly shown, but deposits found on the surface were very hard for the electrons to tunnel through even only very low tunneling current (~30 pA) was applied, indicating that new methods need to be developed to attach fully extended biological molecules to the substrates.

# Résumé

Des méthodes de microscopie à effet tunnel (STM) ont été utilisées pour regarder (a) des monocouches et sous-monocouches auto-assemblées de butanethiol adsorbées sur des films hautement uniformes Au/mica, (b) des molécules d'ADN adsorbés sur différents substrats. De plus, des recherches comportant le traitement des surfaces avant déposition ont été effectuées. Deux solutions fortement oxydantes (acides sulfochromique et piranha) ont été l'objet d'études pour l'élimination des résidus organiques adsorbés sur les substrats d'or. Les traitements des surfaces d'or, à l'aide de l'acide piranha, conduisent à une destruction intense et incontrôlable de la surface provoquant ainsi de sévères perturbations topographiques. L'exposition des surface Au/mica à des solutions d'acide sulfochromique pour une courte durée induit sur la surface des piqurations permanentes atteignant une profondeur maximale d'une couche d'or. Une exposition prolongée de cet acide provoque plutôt une corrosion progressive de la surface jusqu'à la formation d'îlots de 3.3-3.6 Å de hauteur sur une surface autrement plane. Cette piquration contrôlée par l'acide sulfochromique a été utilisée pour la préparation du substrat dans les expériences subséquentes.

Les images STM obtenues pour des monocouches de butanethiol, qui ont atteint l'équilibre, montrent à résolution moléculaire des particularités que nous pensons attribuables aux méthyles terminaux de la surface organique. De grands domaines d'adsorbats organisés et une variante de la structure du super-réseau $p\times\sqrt{3}$ reporté dans des études précédentes, sont observés sur ces surfaces. En utilisant cette nomenclature, la maille élémentaire de la structure reportée ici correspond à $7\times\sqrt{3}$. Les variations latérales en l'élévation des structures endommagées sont associées, sous toute réserve, aux liaisons thiolates sur différents sites (i.e. sites *fcc* et *hcp*) du substrat de Au(111). Contrairement aux études par UHV-STM, il a été possible d'observer des structures moléculaires dans les régions du super-réseau. Ces observations suggèrent que le facteur de remplissage de surfaces qui ont atteint l'équilibre, est très sensible à la méthode de préparation et d'entreposage des échantillons. Les études

des films de sous-monocouches démontrent la formation d'îlots sur la surface d'or. Chaque île possède la même structure observée dans les films de monocouche. La désorption à grande échelle des thiols n'apparaissent pas être une étape nécessaire à la formation de films hautement organisés des systèmes à courtes chaînes quand les solutions de thiols/méthanols sont équilibrées. De plus, la façon de manipuler l'échantillon peut avoir des effets significatifs au point de vue topographique.

Des plasmides naturels de longueur variées et comprenant des séquences d'oligonucléotides modifiées chimiquement ont été étudiés sur des surfaces de graphite et Au/mica. Des images à haute résolution ont été obtenues avec des structures d'hélices clairement résolues. Les dimensions structurales obtenues coïncident aussi avec celles de l'ADN-B. Ce type d'observation moléculaire est très rare; des images de basse résolution des plasmides naturels ne peuvent pas être obtenues de façon routinière. Les modifications des surfaces et les techniques de "combing" moléculaire ont également été employées. La déposition d'absorbats biologiques est clairement démontrée, mais des dépôts trouvés sur la surface rendent difficile l'effet tunnel de passer au travers même avec un courant très faible (~30 pA). Ceci indique qu'il serait avantageux de développer de nouvelles méthodes permettant d'attacher des molécules biologiques sur le substrat dans une forme complètement étendue.

# Introduction

Small structural differences in nucleic acids can have large biological consequences [Watson *et al.* 1987, Saenger 1984]. A single base change can produce a lethal mutation. A slight bend in the backbone or the narrowing of a groove can determine whether a regulatory protein recognizes and binds to a specific site on a DNA molecule or whether a RNA polymerase is capable of transcribing a gene. The comparison of the primary structures of nucleic acids and proteins has been possible with cloning and sequencing technologies, but the detailed spatial information needed to relate primary to higher order structure and function is still lacking. The structural models available are based on X-ray and two-dimensional nuclear magnetic resonance (NMR) studies of a few selected specimens and may represent only a fraction of the variety of structures that exist in a population, or even in a single molecule. The new generation of Scanning Probe Microscopes (SPM), including the Scanning Tunneling Microscope (STM) and the Atomic Force Microscope (AFM), are very attractive tools in biological molecular structure research because of their capability to reveal the three dimensional structure of a surface in atomic resolution, as well as to probe electronic and elastic properties of a truly local nature.

STM and AFM methodologies can have higher resolution than scanning electron microscopy (SEM) in biological molecular imaging because there is little or no reason to coat the specimen with heavy metal layers. The voltage applied to the specimen during scanning in STM is very low (~0.1-1 V in most cases), as opposed to the 5 to 100 kV in SEM, thus minimizing the risk of electron-induced damage. Moreover, the SPM can be operated under vacuum, air, and even aqueous solutions — the natural environment of most biological molecules. Direct observations of structural and even dynamic aspects of macromolecules in their natural environment appear to be possible. Successful images of uncoated DNA molecules have been obtained by STM [Beebe *et al.* 1989, Cricenti *et al.*

1991] and by AFM [Weisenhorn *et al.* 1990, Hegner *et al.* 1993] with widely varying resolutions. But these observations quite often suffer from the poor reproducibility. Uncoated and weakly adsorbed molecules may tend to move or change conformations continually under the scanning force of the STM. In principle, STM requires the use of conductive surfaces in order to measure and stabilize the tunneling current passing from the STM tip to the sample. The mechanism of how electrons could pass through the biological specimen during STM imaging is still not clear since most of the biological specimens intrinsically have poor conductivity. For this reason, the tip-sample separation may be much smaller while imaging biological adsorbates by STM than imaging conductive surfaces; thus the electrical and mechanical forces are stronger and may lead to displaced biological adsorbates. AFM has the advantage of imaging nonconducting surfaces because it is measuring the mechanical forces between the tip and the sample instead of the tunneling current measured in STM [Hansma *et al.* 1988, Bustamante et Keller 1995]. The atomic force measured in AFM is a polynomial function of the tip-sample separation, compared to the tunneling current in STM as an exponential function of that separation. As a result, the resolution of AFM images is usually lower than STM because more atoms of the tip and sample are required to generate the necessary force for AFM imaging. The problem of poor reproducibility also exists in AFM imaging because the weakly adsorbed biological specimens tend to be removed or deformed by the mechanical forces generated during scanning.

To the best of our knowledge, no published methodology has routinely obtained STM images of a biomolecular specimen. Moreover, none of the published results have been reproduced by other groups. Since the main obstacle for this approach lies in specimen preparation, the anchoring of the biological samples and uniformity of the spatial distribution on the substrates becomes very important. Several approaches to this end have been proposed [Allison *et al.* 1990 & 1992, Bottomley *et al.* 1992, Hegner *et al.* 1993, Jing *et al.* 1993, Morozov *et al.* 1993, Rabke-clemmer *et al.* 1994], mainly falling into two categories — surface modifications and adsorbate modifications. These modifications increase the

affinity between adsorbates and substrates by using either chemical or covalent bonds to the surface. Potentiostatic deposition techniques were also applied by some groups [Allen *et al.* 1991, DeRose *et al.* 1991, Lindsay *et al.* 1992]. But until now, very few STM studies have resolved individual DNA molecules routinely; high resolution images are obtained only occasionally. Moreover, none of these techniques were ever successfully applied by other groups. Reproducibility is still the main problem in imaging biological targets.

Due to the intrinsic complexity of this issue, a step-by-step approach was adopted in the present work. It was found in our experiments that the observable coverage is only weakly correlated to the quantity of DNA deposited; the equivalent of 5-10 complete layers in solution are frequentely applied in order to increase the probability of observing isolated molecules. Since locating the adsorbates remains the primary obstacle, imaging adsorbate at higher coverage ( ~ full monolayer) would be appropriate as the first approach. We could then apply the techniques learned from that experiment to sub-monolayer adsorbate coverage, to achieve individual molecular imaging. Alkanethiols were chosen for the first step approach due to (1) their close structural similarities to biological membrane systems and (2) their ability to be chemisorbed onto clean and crystalline gold surfaces via a reaction between Au and S. It is known that this class of organic molecules can form self-assembled monolayers (SAM) on the Au(111) surface. Moreover, these highly ordered, thin organic films has been the subject of enormous scientific interest in recent years because of their potential applications in thin-film sensor devices and optical networks [Dubois *et al.* 92, Swalen *et al.* 87]. The strategy of this approach is to successfully image the organic films in monolayer, sub-monolayer, then biological adsorbates.

# Chapter 1. Principle of STM

## 1.1 Introduction

As the first member of a new generation of microscopes, STM has been proven to be a powerful and unique tool for the determination of the structural and electronic properties of surfaces. The inventors, Gerd Binnig and Heinrich Rohrer of IBM in Zurich, received the Nobel Prize in Physics in 1986. The award was presented only 4 years after the first publication of the STM technique, showing the perceived importance of this new instrument.

The basic idea behind STM is quite simple, as illustrated in Figure 1.1. An extremely sharp conductive tip (ideally terminating in a single atom) is brought close enough to the sample surface that electrons can tunnel quantum mechanically through the barrier

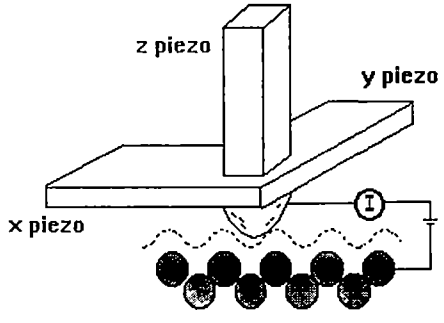


**Figure 1.1** Schematic view of an STM. The tip, shown as a rounded inverted cone, is mounted on a piezo-electric *x*, *y*, *z* scanner. A scan ( dashed line) of the tip over the sample can reveal contours of the surface down to the atomic level.

separating tip and sample. This barrier is influenced by a low bias voltage applied to the tip or the sample (typically a few milivolts to a few volts). The tunneling current, which is approximately proportional to the electron transmission probability of the tunneling barrier between sample and tip, decays exponentially with barrier width $d$ as

$$I \propto exp(-2\kappa d)$$

where $\kappa = \sqrt{2m(V-E)}/\hbar$, $E$ is the energy of the electrons, and $V$ the potential height of the barrier. For tunneling between two metals with a potential difference $\Delta V$ across the gap, only the electrons with $\Delta V$ above or below the Fermi energy can contribute to tunneling [Stroscio & Kaiser 1993]. The electrons within $\Delta V$ below the Fermi level on the negative side tunnel into the empty states within $\Delta V$ above the Fermi level on the positive side. The other states cannot contribute either because there are no occupied higher energy states to tunnel from, or because of the exclusion principle preventing tunneling into already occupied states at lower energy.

Since most work functions for clean metals are approximate 4-5 eV, from the above we find that typically $2\kappa \sim 2\text{Å}^{-1}$. Thus the tunneling current drops by nearly an order of magnitude for every 1 Å of vacuum between the electrodes. The transmission probability for electrons at the Fermi energy is calculated as $\sim 10^{-9}$ by supposing a barrier width as 1 nm[Marti & Amrein 1993]. Such tunneling has a significant probability only for very small barriers (i.e., small tip-sample separation). Achieving such small separations, and keeping the current even moderately stable, requires very precise control of the positions of the electrodes and imposes restrictions, limiting vibrations to less than 0.1 Å.

The position of the tip in three dimensions is accurately controlled by piezoelectric drivers. The tip is scanned in the two lateral dimensions, while a feedback circuit constantly adjusts the tip height, to keep the current constant. A constant current yields roughly a constant tip height, so the shape of the surface is reproduced by the path of the tip, which can be inferred directly from the voltage supplied to the piezoelectric drivers. A single scan records the voltage applied to the *z* piezo as a function of the voltage applied to *(x,y)* piezo. A complete two dimensional image is made of 256-512 scan lines. This feedback-stabilized mode of imaging (called "constant current") is the most common way to get STM images. With computer-based image processing, the data from such scans can be transformed into images that reveal topography as gray level detail, or pseudo-coloured elevation maps.

It is also possible to use a slower feedback response for the tip height, so that the height of the tip remains approximate constant above the average surface, and small atomic features

are reflected in fluctuations of the current, rather than in the tip height. However, this "constant height" mode of imaging is only practical in special cases where the surface is extremely flat. Since the current is so sensitive to the separation of the tip and sample, the "constant height" mode imaging may increase the resolution in $z$ direction.

A measurement of the current-voltage relationship of the tunneling barrier, called I-V curve, is also possible and reflects the electrical property of a specified part surface. The height of the tip is fixed by suspending the feedback loop, and the tunneling current is measured as a function of bias voltages. The electrical properties of different parts of the surface ( i.e., the barrier height) thus can be compared by the different current responses. Such information is particularly useful for surfaces with non-uniform properties.

Since the tip has a finite radius, the surface topography is determined with a finite resolution. Tersoff & Hamann [Tersoff & Hamann 1985] gave a simple way to estimate the resolution as follows: at a given lateral position $x$, relative to the centre of the tip, the height of the corresponding point on the tip is $d = l + x^2 / 2R$ $(x<<R)$, by assuming a parabolic tip with radius of curvature $R$ and the distance of closest approach $l$. As discussed above, the corresponding current in a one-dimensional model is $I(x) \propto \exp(-2\kappa d)$. Since $l$ is constant, thus $I(x) \propto exp(-\kappa x^2 / R)$. Hence the current has a Gaussian profile, with root mean-square width $\sim 0.7(R/\kappa)^{1/2}$. Since $\kappa$ is typically ~1 $Å^{-1}$, even a large tip radius of ~1000 Å gives a rather sharp (though not atomic) resolution of 50 Å.

It is possible to make metal tips with a radius of curvature of a few hundred Å, but not much less. However, because the tunneling current is so sensitive to distance, if the tip is even slightly rough, most of the current will go to whatever atomic scale asperity approaches closest to the surface. It is generally believed that the best STM images result from tunneling to a single atom, or at most a few atoms, on the tip.

## 1.2 STM images

So long as the features are resolved on a nanometer scale or larger, interpretation of the STM image as a surface topograph ( complicated by local variations in barrier height) is generally adequate. But on the atomic scale, it is not even clear what one would mean by a topograph. The most reasonable definition of "topogragh" would be a contour of constant charge density. Only the electrons near the Fermi level contribute to the tunneling in STM, whereas all electrons contribute to the charge density. Thus, on some level, the interpretation of STM images as surface topographs is not adequate. The calculations of Tersoff & Hamann [Tersoff & Hamann 1983 & 1985] have shown that the ideal STM, where the tip end is a mathematical point, is sensitive to the local density of states at $E_F$ (LDOS), i.e., the charge density from states at the Fermi level. But the LDOS is evaluated for the bare surface, i.e., in the absence of the tip, at the position which the tip will occupy. Thus within this model, the coupling between tip and sample was ignored in this interpretation as measuring a property of the bare surface.

More detailed calculations using first-order perturbation theory [Tersoff & Hamann 1983 & 1985] show that this interpretation remains valid, regardless of tip size, so long as the tunneling matrix elements can be adequately approximated by those for an s-wave tip wave function. The tip position is then interpreted as the effective centre of curvature of the tip, i.e., the origin of the s-wave which best approximates the wave functions of the tip. It is also noted that the higher angular momentum components of the tip wave functions (e.g., *p, l,* ... waves) made little difference to the observable Fourier components of typical STM images. But in images of closely-packed metals, these components could indeed affect the image substantially [Chen 1988, 1990]. Later, it was shown [Tersoff 1990] that for a free-electron-like tip (e.g. jellium), the s-wave tip model should accurately describe STM images except in the case of tunneling to band-edge states (e.g., to semi-conducting surfaces at low voltage) and that even then, none but the lowest Fourier component of the image should differ much from the s-wave result.

Theoretical work has been done for the adsorbates on metals modeling the tip ( and the sample) as an atom adsorbed on a model free-electron metal substrate (i.e., the so-called "jellium" model). It was found that the LDOS at the Fermi level for certain adsorbed atoms like helium and oxygen adsorbed on free-electron metals was lower than that for bare metal ; that is, the presence of the atom makes a negative contribution to the LDOS at this energy. This would cause these atoms to look like holes or depressions in the surface in a topographic image. After extremely high atomic resolution was achieved on clean semiconductor and metal surfaces, many attempts were made to perform STM studies on molecules adsorbed on a surface, in order to observe structural information. The most successful attempts have been made in imaging *n*-alkanes and liquid crystals on graphite. While the STM can resolve individual molecules, the mechanism by which insulating molecules adsorbed on the surfaces are imaged is still unclear. One of the first mechanisms proposed was the local modulation of the substrate work function by the presence of the molecules [Spong *et al.* 1989, McGonigal *et al.* 1990, Fisher & Blöchl 1993, Venkataraman *et al.* 1995]. The STM images of the physisorbed molecules do not correspond directly to the electronic structure of the molecules but rather reflect perturbations of the solid substrate electronic states due to interactions between the surface and the adsorbed molecule. Later the STM images of individual Xe atoms were successfully obtained on a Ni(110) surface [Eigler *et al.* 1991] at 4K. While the Xe atom makes virtually no contribution to LDOS at the Fermi level when adsorbed on a metal surface ( its highest occupied molecular orbitals (HOMO) *5p* lies well below the Fermi level of a metal), it appears as a nearly cylindrically symmetric protrusion on the surface. An alternative proposed mechanism involves imaging the molecular orbitals (MO) which have been modified by the interaction between the molecules and the substrate [Nejoh 1990]. Initially it was believed that those orbitals would not be observable because the typical bias voltages used while imaging molecules are far lower than the energy difference between the HOMO and the lowest unoccupied molecular orbital (LUMO) of the adsorbed molecules. However, it has been proposed that the adsorption of these molecules on the surface shifts and spreads the molecular energies to an

extent such that they can be observed by the STM. A third proposed mechanism is based on the resonant tunneling model [Lindsay *et al.* 1990, Mizutani *et al.* 1990]. Resonant states are not normally available, but a MO might extend into resonance near the Fermi level thus making a dominant contribution to an STM image [Eigler *et al.* 1991]. This MO extension may be the consequence of the pressure generated by the tip [Lindsay *et al.* 1990] or by the strong electric field ( on the order of $10^8$ V/m) between tip and sample. Theoretical calculations also show that the tunneling is enhanced by the molecular adsorption [Eigler *et al.* 1991] or the presence a molecular orbital with an eigen-energy close to the Fermi energy ($E_F$ ) of the metal substrate [Lindsay *et al.* 1990].

While atomic images are routinely obtained for physisorbed organic films, the debate is continuing on how to explain these images. The bright stripes visible in STM images of *n*-alkanes are generally believed to correspond to the carbon atoms in the carbon backbone [McGonigal *et al.* 1990 & 1991]. Interestingly, the STM images on graphite are bias voltage-dependent with a voltage threshold 0.3-1 V, which can be varied from trail to trail during scanning [McGonigal *et al.* 1990 & 1991, Mizutani *et al.* 1990]. Above this threshold, molecular images can be obtained, but lowering the bias voltage can result in noisy images or graphite lattice imaging. It was also noted that the lower voltage does not touch or disturb the adsorbates because the molecular images can be obtained again after increasing the bias voltage. The explanation proposed for this observation is based on resonant tunneling model [Mizutani *et al.* 1990].

In addition, STM images show different contrast for different atoms or functional groups [McGonigal *et al.* 1991, Mizutani *et al.* 1990, Spong *et al.* 1989, Venkataraman *et al.* 1995] and even for different conformations [Spong *et al.* 1989, Wawkuschewski *et al.* 1993]. STM images of *n*-alcohol (R-OH) and alkyl chloride (R-Cl) adsorbed on graphite indicate that the OH and Cl functional groups cannot be distinguished from the methylene groups of the hydrocarbon chain attached to them [Buchholz & Rabe 1992,, McGonigal *et al.* 1991, Venkataraman *et al.* 1995]. On the other hand, aromatic rings, cyclo-hexanes in liquid crystals [Mizutani *et al.* 1990, Spong *et al.* 1989], sulfur atoms in alkanethiols (R-SH) and

alkyl disulfides (R-S-S-R) [ Venkataraman *et al.* 1995] have enhanced conductivity compared to the alkyl chains when imaged on graphite, i.e., these functional groups are shown as topographically elevated regions in STM images. Moreover, the cyclic alkane, $(CH_2)_{48}$, also showed the enhanced conductivity at the two folded molecular ends [ Wawkuschewski *et al.* 1993]. Different explanations for these image contrasts have been proposed. Spong *et al.* [Spong *et al.* 1989] suggested that the difference in the contrast between the aromatic rings and alkyl chains in liquid crystal molecules is due to the difference in their molecular polarizabilities, since the magnitude of the work function change on a bare surface of adsorbed molecules is in large measure induced by the molecular polarizability. Another possible explanation is the increase in the local density of states (LDOS) near the Fermi level of the surface due to mixing of molecular and substrate states [Fisher & Blöchl 1993, Wawkuschewski *et al.* 1993 ]. But none of these mechanisms can be universally effective. The explanation of the image contrast of ostensibly "insulating" organic films remains an open question.

Using a jellium model, Lang has found that the higher energy portion of the state density spectrum for a single adatom on a metal surface is reflected in the apparent vertical size of the adatom as a function of bias [Lang 1987]. Interestingly, this study predicts a lowering of the tunnel current over a single sulfur atom because the sulfur pushes some of the metal state density away from the region of the surface where the single sulfur atom sits. This is the opposite of what is observed in the Venkataraman's experiments for sulfur covalently bound in a molecular adsorbate physisorbed on graphite. It indicates, not surprising, that the details of the adsorbate and/or conducting substrate electronic structure are quite critical in determining the nature of the STM images for these weakly coupled surface-adsorbate systems.

## 1.3 STM Design

In scanning tunneling microscopy, a feedback system is used to control the tip-sample spacing ( typically ~10 Å) in order to maintain a stable tunneling junction. A fixed tip-sample bias voltage is applied and the desired tunneling current is selected by the operator. The control system is used to adjust the gap between the tip and sample until that tunneling current is achieved. As mentioned above, the tunneling current is proportional to the transmission probability of the electrons at the Fermi level, which is $\sim 10^{-9}$ between two typical metals. Hence, the reference signal of the control system, the tunneling current, is quite small; usually it is less than 1 nA. In principle, the lower the tunneling current is, the further is the tip from the surface, leading to less perturbations to the surface (or surface adsorbates) induced by the tip. How precisely and rapidly this tiny current is measured directly affects the quality of the instrumentation, i.e., the image resolution and acquisition rate.

As the tip is scanned across the surface, variations in the sample topography and electronic structure affect the tunneling current. The control system must react to bring the current back to the desired value. Since the tunneling current is an exponential function of variations in the gap distance, a log-amplifier is usually needed in the control system to obtain a linear feedback response. Ideally, the adjustments should be made instantaneously and exactly. However, such demands are unrealistic because of the unavoidable time delay and frequency response of the control circuit. If the variations in the tunneling current caused by this non-ideal response function are recorded simultaneously with height information in "constant current" mode, they can offer useful information for surface characterization and analysis.

Vibration isolation is an important aspect of STM where design parameters should be carefully considered. Obviously the normal environmental vibrations (on the level of 1 μm) are much greater than the atomic scale; they are large enough to ruin the tunneling junction. Since the STM is measuring and controlling the tip position to less than an atomic diameter,

the vibration isolation has to damp out noise to the same level. In principle, the STM head should have a compact and rigid form so that it has a high mechanical resonant frequency, and thus it is less sensitive to the low frequency mechanical vibrations. In addition the acoustic-coupling to the tunneling junction through the air is a significant problem in the air-STM system and must be damped out by acoustic isolation.

Although the design and structure of the STM seem simple at first glance, there are subtle aspects that are quite difficult to control. The exacting tolerances for instruments with atomic resolution place a number of constraints on the design. Bringing the tip into tunneling range ( ~10 Å separation) and scanning the tip in a two dimensional raster pattern but without "crashing" it into the sample, requires a precisely designed control system. Stable tips with a single atom at the end need to be reproduced easily and economically. In order to image samples with different characteristics, the STM must be flexible enough to adjust to the differences in topography and conductivity of the various surfaces.

# Chapter 2 Experimental

STM images were obtained using a home-made in-air STM system equipped with a standard piezo-tube scanner and Viton suspension/support for vibration isolation (details in Annex 1). The lateral dimensions were calibrated by the atomically resolved images on graphite surfaces, and vertical heights were calibrated by the 2.36 Å step heights on Au(111) films. The uncertainty of the lateral calibration on small scan areas is 1-5%, and is due principally to non-orthogonalities of the X, Y electrodes of the scan tube. All the images presented herein are formed of a 256×256 matrix of tip heights (or tunneling currents) measured using 12-bit analog-to-digital converters (ADC). The step height can be measured precisely using a histogram of the image and profiles of lines 'drown' across the steps.

Tips were prepared by electrochemical etching of Pt/Ir wire in a 2N KOH/6N KCN solution, or of W wire in 2N NaOH at 8-13 V (ac); no significant differences were observed using the different tip materials, although the yield of Pt/Ir tips were slightly greater than that of W. Most of the images presented herein were obtained in the constant current mode, unless otherwise specified. The +0.1-1.0 V potential was applied to the sample, and the ~0.03-0.3 nA tunneling current was measured at the tip that was maintained at virtual ground. All the images are colour-coded according to the normal gray scale with darker shades corresponding to lower surface elevations. The only image processing that has been applied to these data was a digital background plane subtraction to make the terraced structures of the Au films more clearly visible. In all data presented herein, images obtained during the return sweep of the tip across the surface were identical to those presented here. No evidence of double tips or other imaging artifacts are presented unless otherwise indicated.

Graphite surfaces, both synthetic and natural crystalline forms, *highly oriented pyrolytic graphite* (HOPG) and *single crystal graphite* (SCG), have been used as substrates for molecular adsorption. The clean surfaces were prepared by stripping away the outer layers

with Scotch tape prior to use. The Au/mica films are made according to the method reported by DeRose [DeRose *et al.* 1991]. Mica sheets (Proscience/TechniGlass, ASTM V2) were cleaved to expose a clean crystalline surface, and immediately loaded into an all-metal evaporation chamber pumped by a turbomolecular pump (Leybold). Following chamber evacuation to ~$10^{-7}$ Torr, the mica substrates were heated to ~300-450°C for 4-12 hours in order to degas the crystal surfaces and the vacuum system; ~1500 Å of gold (Johnson-Mathey, 99.999% ) was then evaporated onto the surface at a rate of ~1 Å/sec while maintaining the substrate heating. The Au/mica film was heated for another ~2 hours after evaporation in order to produce uniform and atomically flat surfaces. Samples were stored in sealed polycarbonate dishes prior to use.

"Piranha acid", ***P***, (30% electronic grade $H_2O_2$ : concentrated $H_2SO_4$ = 1:4) was stored in glass containers prior to use. Sulfochromic acid solutions, ***S***, were prepared by dissolution of 5 ml Chromage in 4.0 L of concentrated $H_2SO_4$. Solutions that showed any evidence of suspended solids or abnormal colouration following refrigeration were discarded, although we have noted that the optical density of ***S*** can vary by a factor of two among various preparations; more highly coloured ***S*** solutions were found to produce slightly accelerated surface etching. Both acid solutions were employed in the same manner: Au/mica slides were secured horizontally by the edges of the mica substrate, and the cleaning solution were applied to the upward facing gold surface. The acid solutions remained on the surfaces for times ranging from 30 seconds to 20 minutes, after which time the acid was removed, and the surfaces were rinsed with copious quantifies of ultra-pure $H_2O$. Samples were then rinsed in freshly distilled methanol, then dried under a gentle stream of dry $N_2$ prior to characterization by STM. We have observed the surface modifications of the ***P***-treated surfaces with at least 10 Au/mica substrates and 3 ***P*** preparations, while the effects of ***S*** have been observed with approximately 50 Au/mica samples and 10 ***S*** preparations.

The Au/mica substrates used in butanethiol SAM study were cleaned for 1-5 minutes in ***S*** acid prior to SAM deposition, depending the contaminations on the surface. The acid treating process is known to eliminate organic impurities from the surface, as measured by

the absence of srtuctured infrared absorption bands in the high-frequency 2800-3000 $cm^{-1}$ region of C-H stretches. Butanethiol ($C_4$) SAMs were deposited from 5 μM solutions of butanethiol (Aldrich) in freshly distilled methanol. Deposition was allowed to proceed for several hours, then infrared reflection absorption spectra (IR-RAS) were taken to characterize the films. Solvent bands (~3000 $cm^{-1}$) have never been observed in our IR-RAS results for methanol-based depositions, nor have we observed S-H vibrational modes (~2430 $cm^{-1}$); this indicates that there are negligible quantities of entrapped solvent molecules or non-bonded thiols physisorbed to the substrates. The IR-RAS data obtained in our lab show that $C_4$ films developed in this manner are highly structured, with highly reproducible intensities, bandwidths and band positions [Troung & Rowntree]. Following IR-RAS characterization, these samples were stored in the original thiol/methanol solution until imaged with the STM. For these studies, the +0.1 V sample bias was applied while the tunneling current was kept constant at ~25-40 pA; this corresponds to tunnel junction resistances of 2-4 GΩ. Unlike the high resistance measurements of Schönenberger *et al.* [Schönenberger *et al.* 1995] for long-chain systems, we have not been able to image $C_4$ SAM surfaces using negative sample biases; bare metal surfaces can be reliably imaged under most junction conditions. The resolution of our images is inferior to that obtained using UHV housed STM systems [Porier *et al.* 1994, Porier and Tarlov 1994 & 1995] for similar $C_n$ SAMs; nonetheless, the structures we observe are highly reproducible, and show excellent agreement between the forward and reverse sweeps of the tip across the surface. The structures that we report herein are sufficiently well-resolved that direct comparisons with previous work can be made.

While studying the biological adsorbates, graphite substrates were used as prepared, while the Au/mica films were used in different forms: freshly prepared or modified. The surface modifications can be physical or chemical: (1) ***S*** acid cleaning for 1-5 minutes prior to use, depending on the contamination on the surface, which could create atomic defects on the top layer of the surface (see Chap. 3). (2) chemical modification by immersing the freshly prepared gold films in 5mM 2-dimethylaminoethanethiol ($(CH_3)_2N(CH_2)_2SH$, Aldrich) aqueous solutions for 12 hours.

The oligonucleotides used in our experiment are: (1) 123-ladder double-stranded DNA, (2) ΦX-174 RF I circular supercoiled plasmid (5386 basepairs, Pharmacia Biotech), (3) thiolated poly(Guanine) $G_{50}$ and poly(Adenine) $A_{50}$, which were synthesized by Département de Microbiologie, Université de Sherbrooke. The thiolation links were introduced to the backbone at every other phosphate position. The ladder samples were chosen to provide known length adsorbates, while the plasmid system is more easily detected on the surface due to its large size. The purine-based oligo strands (G,A) were employed because the heterocyclic purine bases may provide stronger Van der Waals interactions with the substrates than the monocyclic pyrimidine bases (U,C,T). In most cases, the sample was deposited in 5-10 μl drops of 5-40 μg/ml aqueous (Nanopure) solutions directly onto the substrates, followed by (1) air drying (deposition method 1) or (2) keeping the sample undisturbed for 6-12 hours at +4 °C in an environment with 100% relative humidity (deposition method 2). Such prolonged treatment did not appear to be advantageous for the chemically modified oligo sequences.

For the chemical modified Au/mica surface, two deposition methods were used: (1) 0.2 μg/ml ΦX-174 RF I plasmid solutions were prepared in 10 mM ammonium acetate buffer solutions. The very diluted solutions were employed because higher concentrations usually cause excessive adsorbate covering [Bottomley *et al.* 1992]. The Au/mica films were then incubated in the solutions for 3 hours at +4°C with the gold side down, where the quantity of the plasmid ranges from sub-monolayer to several monolayers. (2) "molecular combing" [Hu *et al.* 1996]. A small drop of plasmid solution ( ~2 μl) was put directly onto a clean glass coverslip. The coverslip was then carefully laid on top of the modified gold surface with the solution between the two surfaces. The drop spread immediately as the cover glass and the Au/mica film sealed together. After 1-3 minutes, the cover glass was removed and the Au/mica surface was thoroughly rinsed with ultra-pure water and blown dried with dry nitrogen gas. The later technique was shown by Hu *et al.* to make uniform distribution of the deposited specimen, as measured by AFM methods.

# Chapter 3 Results & Discussion

## 3.1 Substrate Preparation Techniques

STM imaging requires the use of conductive substrates in order to measure and stabilize the tunneling current passing from the STM tip to the sample. High resolution images of surfaces and/or adsorbates usually require highly organized surfaces such as the low-index crystal planes of metallic samples. Unfortunately, biomolecular species are only physisorbed weakly to such idealized supports, and there is a tendency for the adsorbate to be displaced by the mechanical scanning action of the STM, or to become trapped at defect sites of the substrate. Highly oriented pyrolytic graphite (HOPG) and evaporated gold films are the most commonly used substrates in working with biological molecules in air and vacuum.

Figure 3.1a is a 750×750 $nm^2$ image of a freshly prepared HOPG surface. As expected, the surface is atomically flat; the atomic flat terraces across the whole image, with only a single atomic step (3.354 Å, the step near the right-bottom corner) and a multiple atomic step (the upper step). Large scale images show that the properly prepared graphite surface can be flat on an atomic scale across areas of several square micrometers. Atomically resolved image can be routinely obtained on such surfaces ( Figure 3.1b). Each white region of the image corresponds to enhanced current measurements in this "constant height" image, and is due to the presence of a single carbon atom on the surfaces; notice that a trigonal structure is observed instead of the known hexagonal lattice structure of graphite crystal. This difference arises from the asymmetry of the three dimensional graphite crystal structure — the carbon atoms in the hexagonal rings on the surface occupy two non-equivalent sites: "A" sites are positioned directly on another atom in the next lower layer, while "B" sites are positioned above a void in this layer (Figure 3.1c). The observed white regions are generally believed to be the carbon atoms at "A" sites, while carbon atoms at "B" sites are invisible in STM images.

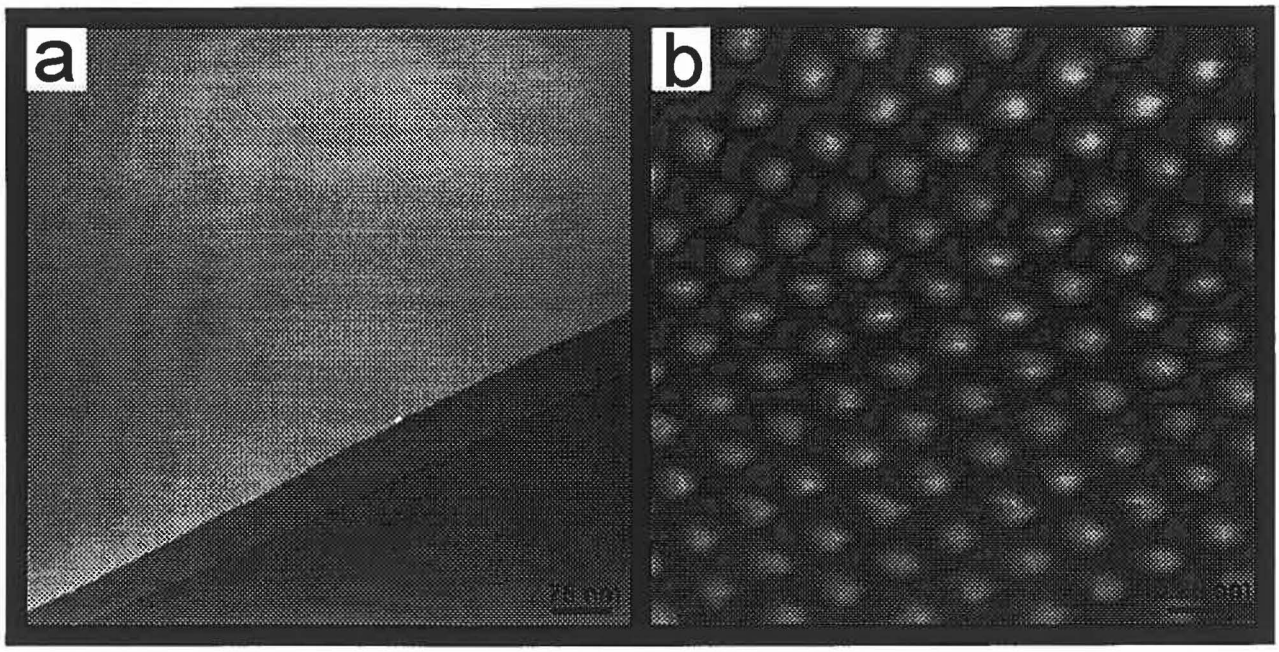


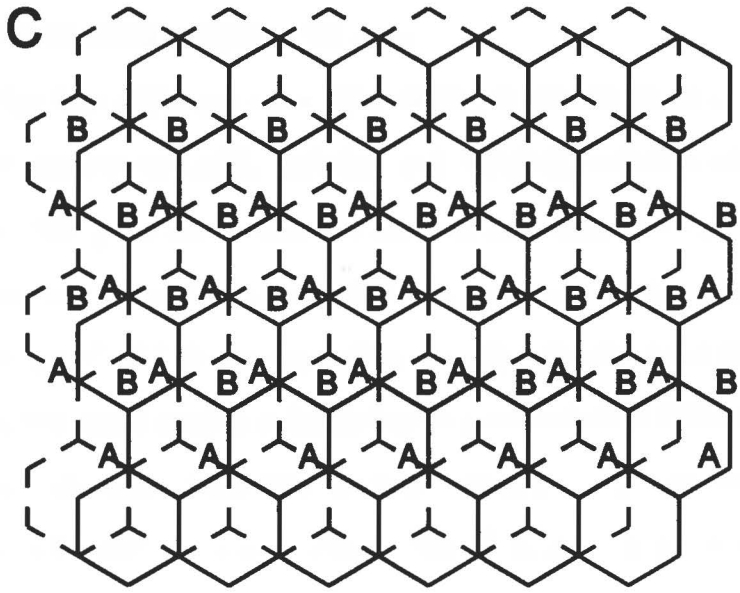


**Figure 3.1** STM images of crystalline graphite surfaces. (a) 750×750 $nm^2$, atomic flat surface with single and multiple steps. (b) 2.5×2.5 $nm^2$ atomically resolved image, in current mode. The (b) image is therefore imaging the current, not the elevation. The gray scale follows the usual convention of brighter areas corresponding to higher elevations. (c) the non-equivalent surface sites on graphite crystal surface.

The nearest neighbor atomic distance in Figure 3.1b is 2.46 Å, which was used to calibrate the lateral dimensions of the scanner.

Though atomic flat graphite surface is ideal for STM imaging, biomolecular species are only physisorbed weakly to such idealized supports. Moreover, defects on such surfaces can be very misleading when they resemble the expected structure of the specimen [Clemmer & Beebe 1991]. Thus our interest shifts to the evaporated gold films, which also offer a relatively inexpensive way to produce large and highly uniform substrates for the study of *n*-alkanethiols. These organic films are then characterized using STM and infrared reflection-adsorption spectroscopy (IR-RAS). Although the gold films are inert to most of chemical reactions, it is not rare to find the adventitiously physiorbed organic impurities on the surfaces. It is essential to minimize the quantity of such adsorbed impurities on this surface, since such artifacts will clearly impede the adsorption of the film constituents, as well as interfere with the spectral analysis of the data.

Several thin film substrates have been employed for the study of the chemisorbed thiol systems, most notably Au/Cr/Si, Au/mica, and Au/glass; recent work by M. Hegner *et al.* [Hegner *et al.* 1993] has shown that the surfaces of "template-stripped" Au/mica samples ( where the experimental surface is that which was deposited directly onto the mica, rather than the surface of the ~100-150 nm metal film) can also provide large flat surfaces for surface adsorption studies, most notably of biomolecular species such as DNA and proteins. We have found that the Au/mica substrates provide extremely reproducible, and extremely flat substrates for molecular deposition, without risk of "binder" layer inter-diffusion with the Au film. Figure 3.2a shows a STM image of a freshly deposited Au/mica surface according to the procedure described in Chapter 2. As expected, the surface is composed of terrace-topped Au domains of 75-200 nm lateral extent, separated by grain boundaries ~15 nm across and several nanometers deep. Previous X-ray diffraction studies have shown that these individual domains are composed of Au crystallites with the exposed terrace surfaces showing largely Au(111) texture [Chidsey *et al.* 1988, Reichelt & Lutz 1971]. Close inspection of the flat terraces reveals the $22 \times \sqrt{3}$ reconstruction of Au(111) surfaces, shown as the "herringbone"

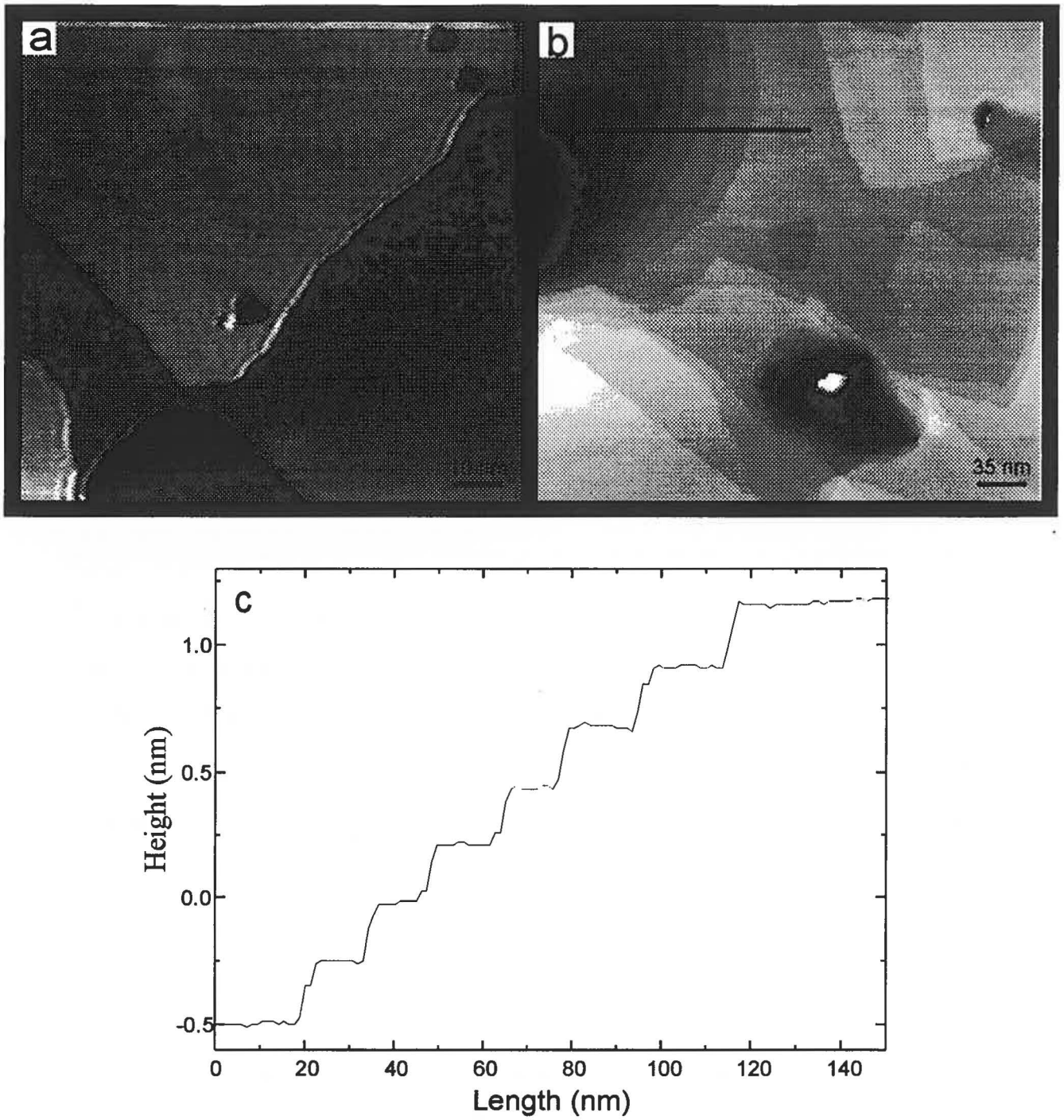


**Figure 3.2** STM image of a freshly prepared Au/mica surface. (a) 100×100 $nm^2$, All the terrace levels present the herringbone $22 \times \sqrt{3}$ reconstruction. (b) 350×350 $nm^2$. (c) The profiles of the line in (b) showing the multiple layers.

patterns on terraces. This reconstruction structure is formed by surface atom rearrangement in order to lower the surface energy, which is characteristic of well-prepared Au(111) surfaces [Barth *et al.* 1990, Harten *et al.* 1985, Hasegawa & Avouris 1992]. This topography is often observed using the evaporation of gold onto freshly cleaved mica surfaces according to our protocols. Of particular note, these surface structures are extremely stable, and show no tendency to be displaced by the scanning action of the tip under normal tunneling conditions or by spontaneous diffusion; Holland-Moritz *et al.* have shown that the mobility of Au/mica surfaces during imaging can be caused by contamination during film evaporation [Holland-Moritz *et al.* 1991]. A large scale image of evaporated Au/mica films is given in Figure 3.2b, which shows the laminar structure of the atomic layers. Figure 3.2c shows the profiles of the line in Figure 3.2b across these step edges, where the multiple layers are clearly observed to be parallel and separated with the 2.36 Å Au(111) step height from each other. The line profiles with the height histograms of the surface are used to calibrate the vertical sensitivity of the scanning tube in our experiments.

In our efforts to optimize the substrate preparation methods, we have found that the limits to sample quality and reproducibility are often imposed by the presence of organic impurities on the surface, rather than the quality of the polycrystalline metallic layer itself. The susceptibility of Au substrates to organic contamination has been documented previously [Bain *et al.* 1989]; it is often presumed that organic species from the ambient environment of the laboratory are weakly adsorbed on the surfaces. This has led us to explore methods of sample preparation by which the surfaces can be reliably cleaned without introducing extensive surface damage that may interfere with molecular adsorption [Kang & Rowntree]. We have attempted to develop methods by which the Au(111) surface can be prepared as routinely as possible, while maintaining the high structure integrity of the substrate that was the original motivation for the now widespread use of Au/mica surfaces. This section will report the effects of acidic solutions (in the absence of specific etchants such as $Cl^-$ and $CN^-$) on the surface topologies of Au/mica films. The first method uses ***P*** acid, as proposed by several publications on SAM formation [Karpovich & Blanchard 1994, Honbo *et al.* 1990,

Pan *et al.* 1996]; the second procedure uses ***S*** acid. Although both solutions can oxidize organic impurities from the surface, as observed using infrared spectroscopy, ***P*** treatments often cause de-lamination of the Au/mica interface. Images taken of Au/mica exposed to pure concentrated $H_2SO_4$ are indistinguishable from that of Figure 3.2, with no evidence of surface modifications or enhanced step mobility. Pure concentrated $H_2SO_4$ had negligible effect on the infrared adsorption bands of adsorbed hydrocarbon contaminates.

Figure 3.3a-d show the Au/mica topography produced by progressively longer exposure to the ***P*** acid solutions (recall that each cleaning stage was followed by extensive rinsing in ultra-pure water). 30 seconds exposure (Figure 3.3a) leads to the formation of isolated island-like features on the Au(111) terraces. These near-circular flat-topped features are typically less than ~10 nm in diameter, with heights that correspond closely to the 2.36 Å step height of Au(111) surface (2.35±0.23 Å, based on 26 individual measurements on 4 substrates). These islands appear to be randomly distributed across the Au surface, with no apparent preference for edges. The vertical dimension of these features strongly suggests that they are Au islands arranged in layers one atom high to produce a Au(111) textured structure; the lateral dimensions correspond to collections of ~1000 atoms per island. The edges of the large terrace structures are frequently more convoluted than found with the "as-deposited" Au film, indicating that the surface has been eroded by the exposure to ***P*** acid, presumably by an oxidation process that leads to substrate dissolution from step edges. Occasionally, the substrate dissolution can start at points other than the step edges, creating atomic holes on the terraces. It can be imagined that the islands on the surface are either additional material that has been deposited onto the Au terraces from the acid solution, or they may be the remains of an almost completely removed layer. We favor the former possibility, since it is unlikely that the highly aggressive P solutions (see below) would cleanly remove almost a complete Au layer with minimal (or no) etching into additional layers of the surface. At this stage of the evolution, it is unusual to find other forms of surface modifications.

After 60 seconds exposure, the Au surface topography is dramatically different (Figure 3.3b). The step edges of the large terrace structures have become much rougher than before,

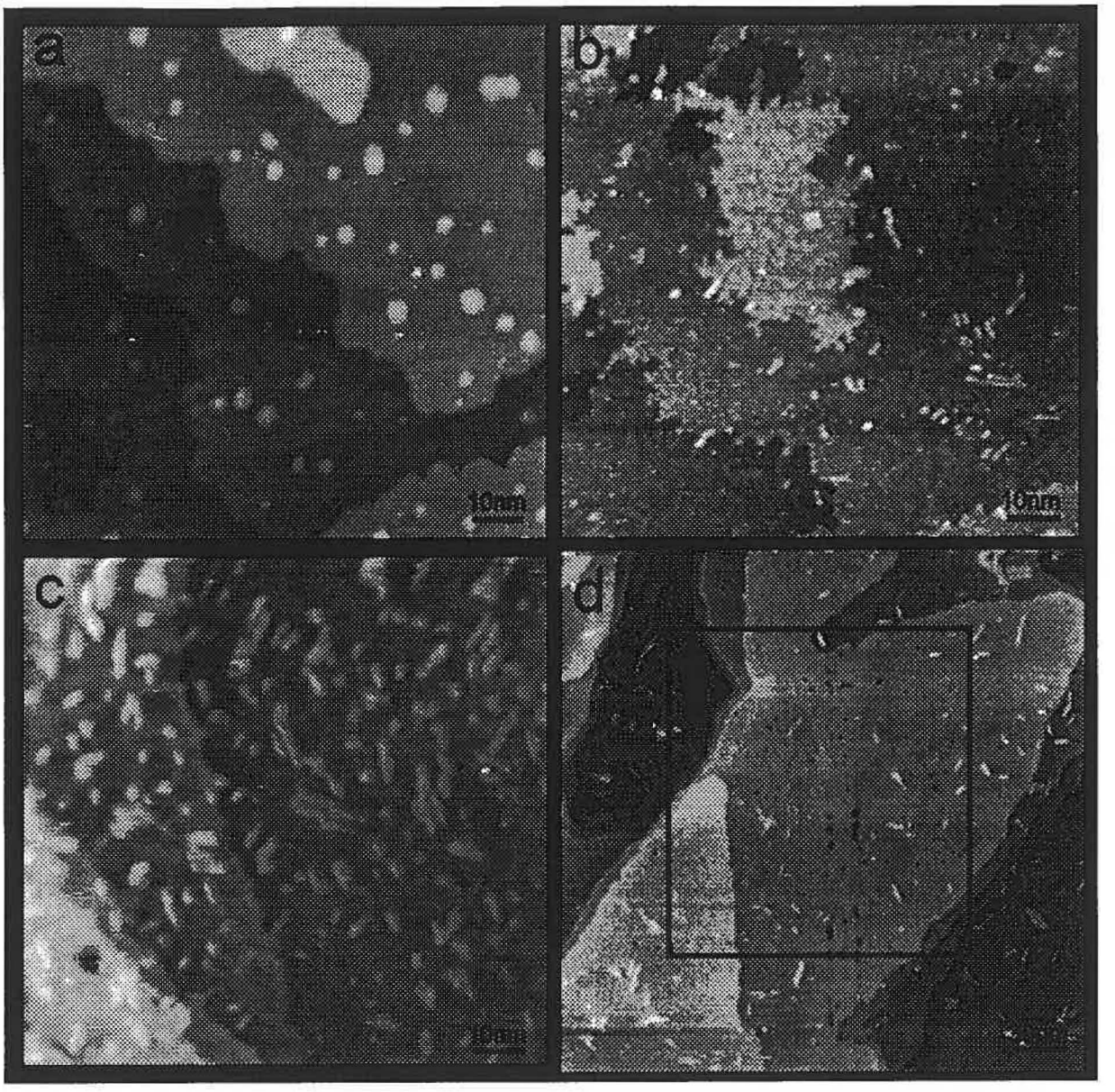


**Figure 3.3** STM images of Au/mica films after exposing to ***P*** acid solution. Exposure time: (a) 30 sec., (b) 60 sec., (c) 135 sec., (d) 195 sec.. Scan size: (a)-(c) 150×150 $nm^2$, (d) 300×300 $nm^2$.

indicating the progress of the ***P*** acid etching. More one-atom-deep holes appear in the middle of the large terraces, with lateral dimensions ~5-15 nm across. The edges of the larger holes and the edges of the large terrace structures are significantly rougher than shown in Figure 3.3a. Meantime, the smaller holes have relatively smooth edges, consistent to the observation that the progressive etching preferentially starts at step edges. Instead of near-circular islands on the surface, "stick-like" objects start to appear, with length ~5-15 nm, width ~2-3 nm. The heights of these "sticks" are 3 to 7 Å, which does not correspond to integer multiples of the fundamental 2.36 Å step height of Au(111) surface. No preferential orientation for these objects with respect to the substrate or scan direction was observed. It is possible that the islands in Figure 3.3a are the favorable sites for later depositions from the solutions to form non-crystalline three dimensional aggregates. We do not believe that these three-dimensional objects are directly deposited "as-is" from solution since they are never observed during the initial stages of Au(111) exposure to the ***P*** solutions. Furthermore, the size distribution of these objects is clearly a function of time, as shown below. The stick-like objects are reproducibly observed even while avoiding direct contact between the ***P*** solution and the mica edges of the gold film, demonstrating that the observed structures are not silicates or aluminates removed from the mineral substrates.

The surface morphology continues to degrade during extending the exposure of the Au surface to the ***P*** acid solution. 135 seconds acid etching leads to "cigar-like" images (Figure 3.3c). These "cigar-like" objects distribute on the surface randomly, no object across step edges were ever observed. The measurements of the vertical dimension show that they are ~ 5-10 Å high ( i.e., ~2-3 Å higher than the objects in Figure 3.3b), indicating continuing deposition onto the pre-existing structures. It is interesting to notice that the size distribution of these particles is remarkably narrow, with typical length:width:height ratios of ~10:2:1. This anisotropic three-dimensional growth is in clear contrast with the normal two-dimensional growth of gold-on-gold, and indicates that the composition of the particles differs significantly from that of the substrate. Figure 3.3d is a typical large scale Au surface image after 195 seconds ***P*** acid etching. The objects on the surface are progressively larger and

higher, ~10-25 nm in length and ~7-9 Å in height. Moreover, these objects were no longer mechanically stable during the scanning process; the centre region of this image (within the marked frame) has fewer structures because many of them have been removed by previous imaging in this region. In these later stages, the etching principally took place on the middle of the terraces rather than the step edges, as indicated by the relatively smooth step edges and numerous etching holes on the terraces. This leads us to propose that the gold aggregates and the terrace edges may have been oxidized after 1 minute exposure to ***P*** acid solutions, but this needs to be confirmed by further study with other methods such as SEM, X-ray photon-electron spectroscopy etc.

In our experiments with ***P*** acid etching, it was found that this "standard" surface cleaning process is aggressive and difficult to control. While exposed to ***P*** acid solutions, the Au(111) surfaces change their morphology quickly and usually have numerous objects with height several times more than the step height of Au(111) surface. The anisotropic structure of these aggregates strongly suggests that the forces adhering the object to the surface are significantly weaker than the cohesion forces with the aggregate, and that these particles are not pure gold. For these reasons, we have explored and adopted the use of sulfochromic (***S***) solutions, where the surface etching process of Au(111) surfaces is far more controlled and less aggressive than that in ***P*** acid solutions. Figure 3.4a gives an image of the Au/mica surface after 1 min ***S*** etching. The large, flat terraces of the Au(111) surface are still clearly visible, with one-atom deep etching pits spreading on them. Unlike ***P*** acid treatment, there is apparently no preferential step-etching of gold in ***S*** acid solutions, as indicated by the relatively smooth step edges, and the striking differences between Figure 3.3a and Figure 3.4a. It is possible that if such etch-pits were created, they could be rapidly refilled if there was a significantly large number of mobile gold atoms available. However, the mechanical stability of the Au/mica surfaces at this stage (as evidenced by lack of imaging-related structural changes, regardless of tunneling resistance in the 0.5-3 GΩ) indicates that there are very few mobile gold atoms at this point, and that the step edges are relatively insensitive to the ***S*** solution. The etch pits are irregularly shaped, with no specific orientations observed with respect to the crystal lattice, as

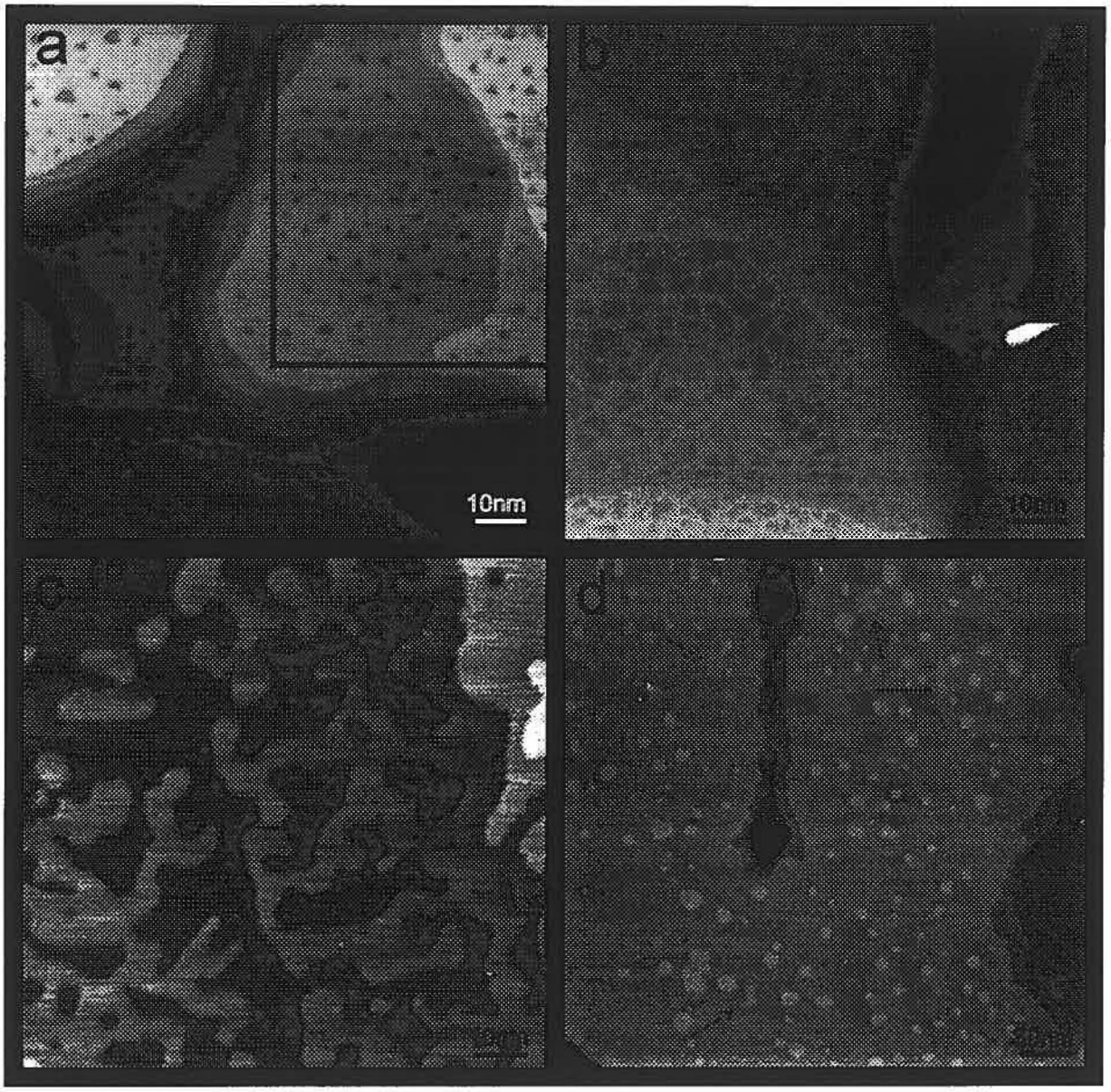


**Figure 3.4** STM images of Au/mica films after exposing to ***S*** acid solution. Exposure time: (a) 1 min., (b) 2 min., (c) 5 min., (d) 10 min. Scan size: (a)-(b) 200×200 $nm^2$, (c) 100×100 $nm^2$, (d) 300×300 $nm^2$.

was reported previously for Au(111) surface reaction with aqueous $CN^-$ [McCarley & Bard 1992]. The pits are exclusively one-atom deep (i.e., there are no "holes-in-holes"), with a mean diameter of ~5 nm. They are almost uniformly distributed on the topmost terraces, with a possible "avoidance" of pit-formation near the downward-leading step edges. Figure 3.5 gives the surface height histogram of the upper-right portion in Figure 3.4a (marked by a frame) with etching pits; the step height agrees well the theoretical value 2.36 Å. The small peak on the left in this figure represents the portion of etching pits, which is one atomic layer lower than the terrace they occupy. The pits coverage was then calculated as ~10% of the surface according to a similar histogram of the large terrace. Although these pits appear to be quasi-randomly distributed across the topmost layers, this is clearly not true for successively lower levels of the topography. For example, the lower terrace in the bottom-left corner of figure 3.4a (not the trench) has significantly fewer etching holes near the steep step edges leading up to the main terrace region. The pits in these lower surface regions remain one-atom deep, but the mean diameter is now ~2-3 nm, and smaller yet for pits located near the step edges. Furthermore, there are virtually no etching pits in the trench area on the terraces at still lower elevations as shown in the middle-left edge of Figure 3.4a. These propensities have been reproducibly observed for many samples and several ***S*** preparations. It is also interesting to notice that although ***P***-treated Au/mica shows extensive deposition of island structure within 30 seconds, no additional material deposition was observed on ***S*** -treated gold surfaces in the first ~5 minutes of exposure. One possible explanation is that the dissolved gold is better solvated by the chromic acid solution, and therefore is less reactive to the gold surface in ***S*** acid solutions than when dissolved in ***P*** acid solutions. These solvated species would remain in the ***S*** acid solution and not return to the surface, leading to well controlled surface morphology.

If the exposure time extends to 2 minutes, these small etching pits become larger with lateral dimensions from several nanometers to dozens of nanometers (Figure 3.4b). The height difference between the top surface and the bottom of these holes remains consistent with the 2.36 Å Au(111) step height. Since there is no preferential step etching, we believe

that these larger holes were resulted from the convergence of the randomly distributed smaller etch pits shown in Figure 3.4a. The dissolved portion have increased to about 55% of the total surface area, leading to a "net-like" appearance. The anisotropic etching rates of the various surface terraces are also noticed this image, as observed previously in Figure 3.4a. The trench area (darker area across the right part of the image) is 5-8 atomic levels below the main terrace structure, and it has a significantly lower etching rate than other parts, as indicated by fewer etching pits found in the deeper regions of Au/mica surface. We consistently found that there are fewer etching pits for the steeper regions leading down to narrow trench regions. Apparently, the geometry of the surface structure leads to this anisotropic surface etching. There are two possibilities for this observation: (1) Since the trench area is formed as a nearly closed basin with ~1-3 nm height, the diffusion of the acid may be slower in this region, such that the overall oxidation rate is lower and dissolution is more difficult. (2) there may be some residual air trapped in this trench area while the acid covers the surface. The air would be compressed when the acid was decending toward the bottom of the trench area. It may take some time for the residual air to escape from the acid-covered surface, thus retarding the etching procedure. The absence of "holes in hole" in all of these images is consistent with this observed anisotropic etching, since each hole can be regarded as a very small trench.

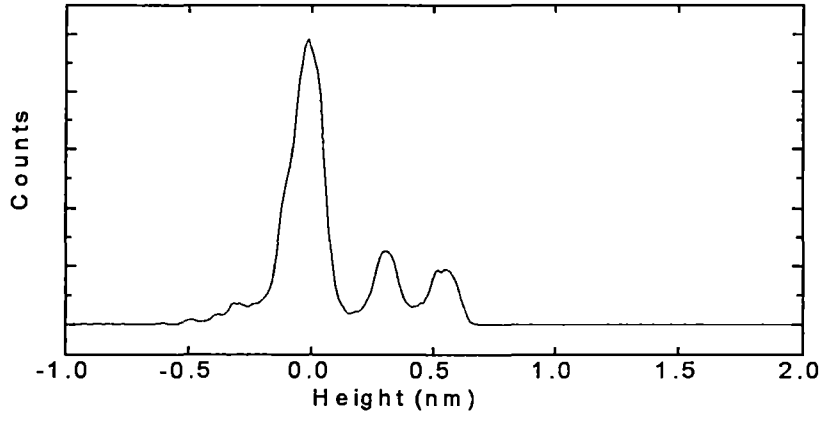


**Figure 3.5** The height histogram of the upper-right part in Figure 3.4a of Au/mica films after exposing to *S* acid solution.

The surface morphology continues to evolve after 5 min etching in ***S*** acid solutions (Figure 3.4c). The dissolution has proceeded; the etching holes have continued their aggregation/growth. The breaking of many links of the "net-like" structures leads to the "worm-like" structures and highly convoluted topologies. It is difficult to measure how much of the Au layer was dissolved at this stage because near the steps, the second layer which was completely exposed after etching cannot be distinguished from the other parts of the same terrace. Surprisingly, the step heights of these "worm-like" islands are not uniform; although some are equal or less than the Au(111) step height, most are varied from 2.8Å to 3.1Å. this is the first evidence of a chemical modification of the surface within the surface layers; specifically-adsorbed anions or physisorbed species on the surface would be found with equal probability on and within the net structures, leading to no discernible variations in step height. It can be imagined that this modification results in a physically different step height, or it may modify the electric structure of the surface so as to decrease the barrier to electron-tunneling, thus increasing the junction width (i.e., the probe height) in a constant-current imaging mode. We reject the later possibility for an oxidized surface, since the work-function of the oxidized surface would be greater than that of the pure gold surface, thus decreasing the tunneling probability for a fixed tip-surface separation. We thus conclude that the apparent height increase of the "worm-like" structures above the sub-level gold planes is the result of a topographically thicker single-layer structure. It is highly unlikely that it is an under-estimated thickness of a bilayer structure, since as discussed above, we have never observed hole-in-hole structures that would be required to produce such bilayer structures.

Increased exposure to ***S*** solutions can result in a more complete and highly anisotropic dissolution of the Au(111) surface. Figure 3.4d shows although most of the top terraces has been dissolved after ~10 min exposure to the ***S*** acid solution, the etching does not continue into sub-layers; this results in a highly planar topography with small isolated island-like structures. These structures are nearly circular, with typical diameter of ~10-15 nm. Although this topography appears to be very similar to that produced by very short exposure of the Au/mica surfaces to ***P*** solutions (Figure 3.3a), the vertical dimensions of these surfaces

are significantly and systematically different in three aspects. Firstly, the islands are 3.3-3.6 Å high, which is 40-50% higher than the Au(111) step height. The height discrepancy cannot be the result of calibration error, since the vertical calibration uncertainty of the scanner is better than 5%, and images of freshly prepared Au(111) surfaces measured immediately before and after these experiment found the expected 2.36 Å vertical step height. The progressively increasing height of the super-structures confirms that these island structures are the result of the continued erosion of the "net-like" structures shown in Figure 3.4b,c, rather than being the result of material deposition from solution onto the gold surface, as postulated for the initial stages of the ***P***-etching process shown in Figure 3.3a. The second difference with respect to Figure 3.3a (and with respect to fresh Au/mica surfaces) is the presence of small protrusions on the surface with elevations of only ~1.2-1.6 Å (well below the standard 2.36 Å Au(111) step height); examples of these structures are identified with arrows on Figure 3.4d. Although small, irregular and never comprising more than ~5% of the total surface area, these features are very reproducible and are equally visible in data taken on the reverse-passage of the STM tip across the surface. The tunneling current (measured simultaneously with the topographic data) shows no anomalous behaivor that would indicate an unstable tunneling junction in these regions. Thirdly, it is interesting to note that the topmost terrace of Figure 3.4d is separated from the next-lower level by the same 3.3-3.6 Å observed for the islands heights, indicating the etching of the remnants of the top-layer that produces the island-structures has also modified the planar regions of the main terrace levels, leading to physically thick layers. The steps within the trench area ( the centre-top region of Figure 3.4d) are consistently ~2.4 Å high, indicating that these regions are relatively unaffected by the ***S*** acid. Just as the etching process is demonstrably slower in the trench area, the chemical modifications that lead to anomalous step heights in these regions are also slower with respect to the relatively exposed regions. Although the main terrace shown in Figure 3.4d is extremely flat, it is difficult to determine conclusively that this terrace is planar (within 1.2 Å elevation) across the entire 300 nm surface. This makes it difficult to ascertain if the increased step-heights

observed at the edges of the top-most terrace imply that the layer itself is uniformly 3.3-3.6 Å thick, or if the terrace layer expansion is restricted to the vicinity of the edges.

Further exposure to the ***S*** acid solutions does not change the surface topography significantly, i.e., the island-like structures remain with 3.3-3.6Å height, and the step heights leading to the topmost terrace are consistently greater than that of the original Au(111) steps. The apparent stability with respect to further dissolution shows the oxidized surface is chemically stable and increasing difficult to etch in the ***S*** solutions. Figure 3.6 is an image of Au(111) surface after 15 min exposure to the ***S*** acid. The atomic etching holes appear on the surface again, which promotes the progress of etching. But the etching rate now is much slower than before, shown as less holes on the surface at this stage. Meantime, the surface morphology is becoming mechanically unstable if the tunneling resistance is under 3.3 GΩ (Recall that the normal tunneling resistance was ~1 GΩ in these studies). The islands are converged or displaced to step edges after scanning, while at the same time the step edges are becoming crenulated, similar to those observed on organic SAM on gold [Bucher *et al.* 1994, McCarley *et al.* 1993]. The center and upper-right regions in Figure 3.6 (regions in frame) show such changes, which have similar morphology as other regions before. Before this image was measured, 3 and 8 images for center and upper-right regions respectively have been obtained under normal tunneling conditions, i.e., with bias 0.25 V and current ~0.3 nA, which corresponds tunneling resistance ~833 MΩ. No such morphological change was observed with time in our experiments.

In the experiment of ***S*** acid treatment, all the images are quite stable while stored in petri boxes for more than one day, not time dependent [McCarley and *Bard* 1992, Venkataraman *et al.* 1995]. This is also true under most of the tunneling conditions. But the worm-like and island-like images are less stable while the tunneling resistances are below 3.3 GΩ. The decrease of the tip-sample bias or increase of the tunneling current will cause remarkable changes of those surfaces during scanning. The lower the tip-sample bias (e.g., from 0.5 V to 0.1 V), or the higher the tunneling current, the more rapidly the surface topography changed by scanning. Under the same tunneling conditions, the "worm-like" structures are less

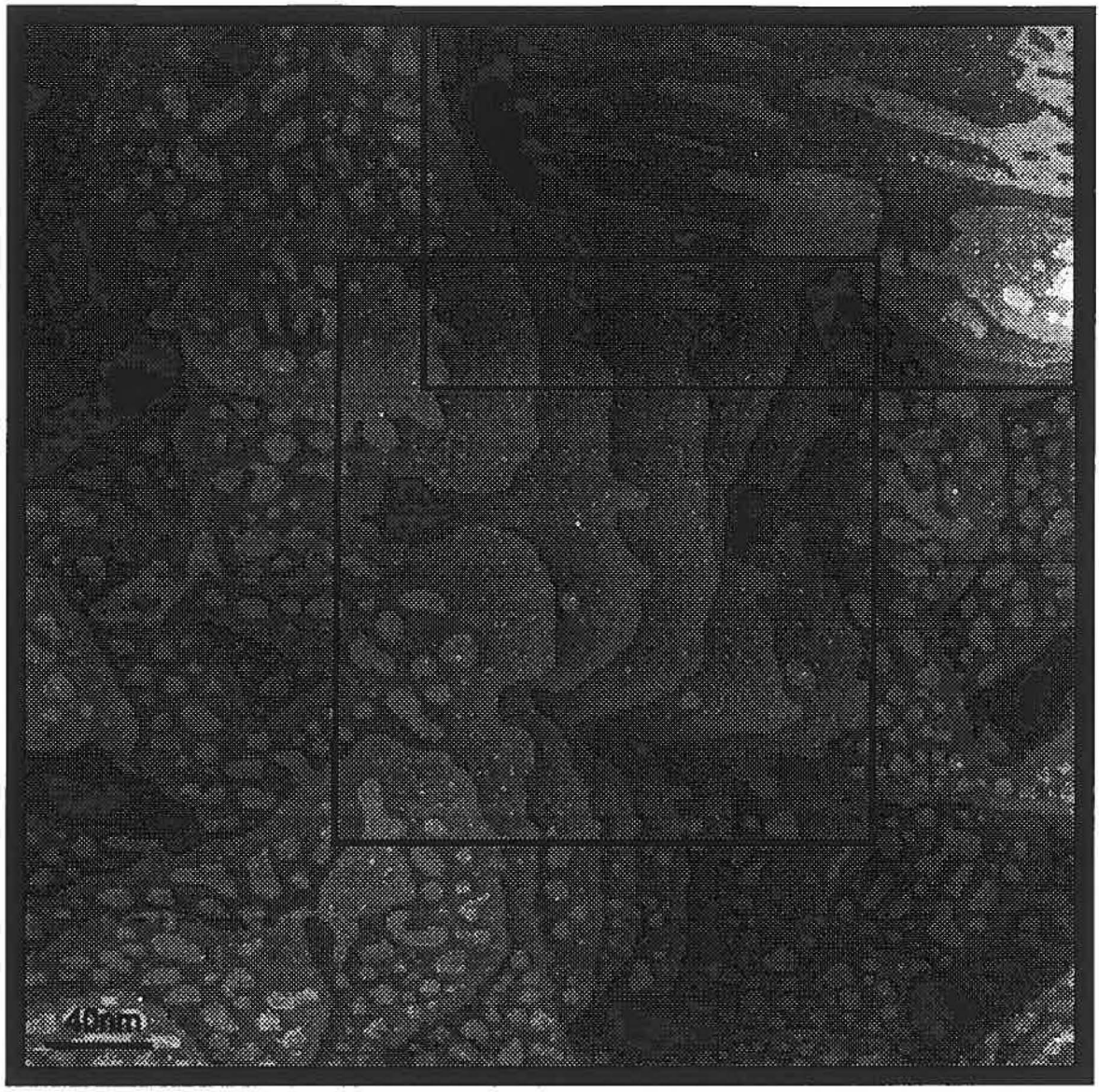


**Figure 3.6** Au/mica surface after 15 min exposure to ***S*** acid solution. Scan size: 400×400 $nm^2$, Bias: 1.0 V, Current 0.3 nA. Before this image was acquired, 3 and 8 images for center and upper-right regions respectively were measured under normal tunneling conditions, i.e. with bias 0.25 V and current ~0.3 nA, which corresponds tunneling resistance ~ 833 MΩ.

affected by scanning than that for "island-like" structures. There are two possible explanations for this observation. First, the tip-sample separation may be much smaller on "worm-like" and "island-like" Au/mica surfaces because the partial oxidation of gold makes such surfaces difficult to tunneling through, i.e., lower probability of electrons passing the tunneling barrier. The "worm-like" surfaces may have lower oxidation coverage than the "island-like" surfaces from the vertical dimensions measured; yet they are more stable. The second possibility is related to the geometry of the surface. The islands on the terraces on island-like surfaces are separated from each other, while the top layer on other surfaces (with atomic holes and worm-like) is connected like a net. The stronger inter-atomic interactions on the more complete top surface may prevent the atoms from being displaced by scanning.

From the results presented above, significant surface modifications were observed after exposing Au/mica surfaces to ***P*** and ***S*** acid solutions. With ***P*** acid treatment, the gold surfaces were oxidized and dissolved quickly, with part of the dissolved gold returning to the surface in various and uncontrolled structural forms. This procedure is hard to control due to the aggressive etching. While exposing to ***S*** acid, the gold surface undergoes well-controlled modifications, being oxidized and dissolved layer by layer, apparently leading to the complete oxidation of the top layer. Unlike the case for ***P*** solution treatment, we have found no conclusive evidence indicating that re-deposition of etched material back onto the surface is a significant process in ***S*** acid treatment. Two possibilities were suggested for the well-controlled etching procedure of ***S*** acid: (1) the gold oxidation may be more resistant to dissolution by ***S*** acid than ***P*** acid, (2) the dissolved gold ions are less reactive to the Au surface in ***S*** acid solutions. To the best of our knowledge, this is the first STM study of the "standard" cleaning process for Au(111) surface. The molecular characterization of surface modifications may promote explanations for some inconsistent observations in various studies where these pre-cleaned gold films are used.

We have studied the morphological modifications of Au/mica substrates after exposure to piranha and sulfochromic acid solutions using STM methods. While the acid treatments could remove the organic contaminates from the surface with varying degrees of success, defects

were inevitably introduced into the surface structures. The exposure of Au/mica films to piranha acid leads to extensive and uncontrolled etching of the surface within 30 seconds, and severe disruption of the surface topography; extended exposure causes the precipitation of material on the surface that is easily displaced by the STM. Au/mica films are also readily de-laminated using these solutions. Exposure of the Au/mica surfaces to sulfochromic acid for less than 300 seconds leads to the formation of permanent etch pits of the surface that are exclusively one Au layer deep; extended exposure leads to progressive lateral etching of the surface, ultimately leading to the formation of 3.3-3.6 Å high islands on the otherwise flat surface, increasing levels of surface oxidation, and mechanical instabilities under the scanning action of the STM tip. The IR-RAS results also indicate that exposure of Au/mica surfaces to sulfochromic acid for 1-5 minutes is a highly effective cleaning procedure for the elimination of hydrocarbon contaminates, while minimizing the chemical and structural modifications of these substrates. Such surface defects will not interfere with molecular adsorption when the acid treated substrates are used. The acid treatment study offers a new way of gold substrate preparations for use in organic thin-film deposition studies. Furthermore the atomic defects on the surface created by this selective etching method can also be used to physically anchor the bio-molecules with minimum deformation thus give higher resolution in scanning-probe investigations. This well-controlled sulfochromic acid etching procedure was used for the substrate preparation in subsequent experiments.

## 3.2 Molecularly Resolved Self-Assembled Butanethiol Monolayers on Gold

### 3.2.1 Introduction

Self-assembled monolayers (SAMs) of organic species chemisorbed to metal and semiconductor surfaces have attracted enormous attention in recent years [Dubois *et al.* 1992, Swalen *et al.* 1987, Ulman 1991] due to their conceptual simplicity, ease of preparation, and the unusually high structural integrity that can be produced at the organic-substrate interface [Fenter *et al.* 1994, Strong & Whitesides 1988], in the 'bulk' phase of the organic film [Bain *et al.* 1989, Porter *et al.* 1987], and at the surface [Alves *et al.* 1992, Camillone *et al.* 1994, Chidsey *et al.* 1989, Schönenberger *et al.* 1995, Widrig *et al.* 1991]. In particular, the adsorption of organothiols (or disulfides) from solutions onto gold substrates is a reliable method for robust film preparation and surface functionalization; most of the work to date has been on the structural characterization of the thiol/Au(111) systems. The structural aspects of SAMs have been extensively explored using macroscopic analytical methods to investigate the 'bulk' phases (e.g., infrared reflection absorption spectroscopy (IR-RAS) [Bain *et al.* 1989, Porter *et al.* 1987, Truong & Rowntree], surface wetting measurements [Bain *et al.* 1989], ellipsometry [Bain *et al.* 1989]) and microscopic probes to investigate the surface structures (e.g., STM [Poirier *et al.* 1994, Poirier & Tarlov 1994 &1995, Widrig *et al.* 1991], AFM [Alves *et al.* 1992]); detailed structural descriptions of these organic systems have also been obtained by electron [Dubois *et al.* 1993], atom [Camillone *et al.* 1993 & 1994, Chidsey *et al.* 1989] and X-ray diffraction studies [Fenter *et al.* 1994]. In the case of $CH_3(CH_2)_{n-1}S$-Au systems ($C_n$ SAMS), the commonly assumed structural model is deceptively simple: the thiols are presumed to be adsorbed as thiolates (or if oxidized, as sulfonates [Li *et al.* 1992]) with the sulfur atoms adsorbed into three-fold hollow sites of the Au(111) surface, with the organic chains extending away from the surface with tilt and twist angles determined by the ability of the chains to form compact structures resembling bulk alkane phases. The S-Au

interface in this simple model has adjacent sulfur atoms arranged on a $\sqrt{3}\times\sqrt{3}R30^{O}$ superlattice of the underlying Au(111) surface, with inter-sulfur distances of 4.99 Å; all adsorption within an ordered domain occurs at identical *hcp* or *fcc* three-fold hollow sites of the Au(111) lattice. This structure has also been observed at the methyl terminated surfaces studied by atom diffraction [Chidsey *et al.* 1989] and STM with ultrahigh tunneling resistances[Schönenberger *et al.* 1995].

As increasingly sophisticated experimental and theoretical investigations have shown, however, this model of a well-ordered and highly uniform adsorbed phase appears to be an inadequate description of these systems, especially at temperatures ≥300 K [Bensebaa *et al.* 1995]. Insofar as these films have enormous potential for the development of opto-electronics, sensor devices, etc., [Dubois *et al.* 1992, Swalen *et al.* 1987, Ulman 1991] there is an ongoing need for improved structural and dynamical descriptions of these films. Recent X-ray diffraction measurements by Fenter *et al.* [Fenter *et al.* 1994] suggest that adjacent sulfur atoms may dimerize to form a covalently linked disulfide, with a S-S distance of ~2.2 Å, corresponding to occupancy of one three-fold hollow site and a nearby bridge site, rather than the more commonly assumed next-nearest neighbor three-fold hollow sites separated by 4.99 Å; this S-Au conformation can be reconciled with the 'bulk' and surface structural information collected to date if *gauche* defect sites are introduced at the methylene groups closest to the sulfur atoms. It now appears that the $\sqrt{3}\times\sqrt{3}R30^{O}$ structures of the *surface* are also subject to reinterpretation, depending on the sample preparation method, chain length, etc. Two particular superstructures of the methyl-terminated surfaces have recently been characterized. The first is the *c(4×2)* superlattice of the basic $\sqrt{3}\times\sqrt{3}R30^{O}$ structure that has been observed for long chain ($C_{8-12}$) adsorbates using helium atom diffraction [Camillone *et al.* 1993], and more recently, by STM images of the surfaces of long-chain SAMs [Camillone *et al.* 1994, Delamarche *et al.* 1994, Poirier & Tarlov 1994, Schönenberger *et al.* 1995]. This 8.5 Å×10.1 Å rectangular unit cell appears to be the thermodynamically stable structure for full monolayers of long-chain $C_n$/Au(111) systems; these structures can be produced by thermal annealing of the basic $\sqrt{3}\times\sqrt{3}R30^{O}$ surfaces to

~50 $^{O}$C. When long-chain SAMs are thermally annealed to ~100 $^{O}$C, they can form $p\times\sqrt{3}$ pinstripes of a lower surface density [Camillone *et al.* 1994] than the original *c(4×2)* structure, implying that the restructuring is accompanied by the desorption of some of the chemisorbed thiolates. Poirier *et al.* have used UHV-STM methods [Poirier *et al.* 1994, Poirier & Tarlov 1995] to show that a $p\times\sqrt{3}$ pinstripe structure can crystallize *directly* from the initially disordered adsorbed phase of short-chain $C_4$/Au(111). This crystallization leads to domains (~10-30 nm lateral dimensions) of well-organized adsorbates that appear as pairs of parallel 'tracks' in the STM images, with each pair being imaged as a pinstripe; this structure will be discussed in more details below. Most important in the context of the present study was the observation that *between* the sets of track structures (i.e., between the pinstripes), there was no evidence of chemisorbed thiolates; no molecular structure was observed *within* the pinstripe either, but the elevation was ~0.5 Å greater than that measured in the inter-pinstripe region. Dubois *et al.* [Dubois *et al.* 1993] have studied the structures of $C_4$ SAMs deposited (and equilibrated) under UHV conditions using low-current LEED, and have found structures that were indexed as $4\sqrt{3}\times\sqrt{3}R30^{O}$ and $5\sqrt{3}\times\sqrt{3}R30^{O}$. These unit cell structures are missing at least one complete thiolate row.

These reinterpretations of SAM surface structures are of crucial importance in the organothiol film study because they indicate (1) that large fractions of the fully equilibrated surfaces may be devoid of chemisorbed thiols, (2) that the desorption of thiols is required to form the $p\times\sqrt{3}$ phases, and (3) that the low-density $p\times\sqrt{3}$ phases are the thermodynamically stable structures for these short-chain systems at room temperature, just as it was found for the longer-chain systems prepared by sample annealing.

In IR-RAS investigations of butanethiol monolayers in our lab [Truong & Rowntree], the mechanisms for film growth, and the factors that determine the quality of the final film have been examined; the changes in the IR-RAS spectra during the film's structural evolution were used to assess the average film structure and the molecular orientations, and provided evidence for island formation during film growth. No evidence was found for extensive desorption of the thiolates into solution, nor for adsorption/desorption equilibria. The $C_4$

SAMs imaged by STM in this work were prepared and equilibrated using conventional solution-phase techniques. A relatively dense striped phase has been observed [Kand & Rowntree 1996], which is similar to the $p\times\sqrt{3}$ structures reported previously by Poirier *et al.* [Poirier *et al.* 1994, Poirier & Tarlov 1995], albeit with a shorter repeat length '*p*' perpendicular to the main stripe axis. More importantly, the images presented here show molecular structures in regions between the parallel track structures that are structureless in the UHV-processed surfaces, and were previously reported to be devoid of thiolates. These structural differences will have important consequences for measurements of surface coverages, and for applications that require the preparation of highly uniform and defect-free surfaces.

### 3.2.2 Results

STM images taken ~24-48 hours after film deposition show the growth of 'crystalline' domains at the expense of the disordered 'liquid' like phase, as reported by Poirier *et al.* [Poirier *et al.* 1994, Poirier & Tarlov 1995]. In the case of $C_4$ SAMs that have been allowed to equilibrate in the butanethiol/methanol solution, the fully evolved film structures show a well-resolved striped phase. Figure 3.7a shows a typical 75×75 $nm^2$ STM image of these structures. As expected from the use of extremely uniform gold films and the ability of thiol adsorption to reduce the surface defect density [Poirier & Tarlov 1995], the surface of the SAM is highly planar, with large terraces separated by steps of the gold substrate. On all terraces, individual striped domains are observed on the three equivalent high-symmetry directions of the underlying Au(111) lattice, showing that the domain growth is crystallized by widely separated points on the Au substrate. The interfacial boundaries between the individual domains introduce disordered regions approximately 1-3 nm wide; these regions are often elevated above the well-ordered domain regions of the surface by 0.2-0.5 Å. The stripes are consistently spaced in these images. It has been observed that extended exposure

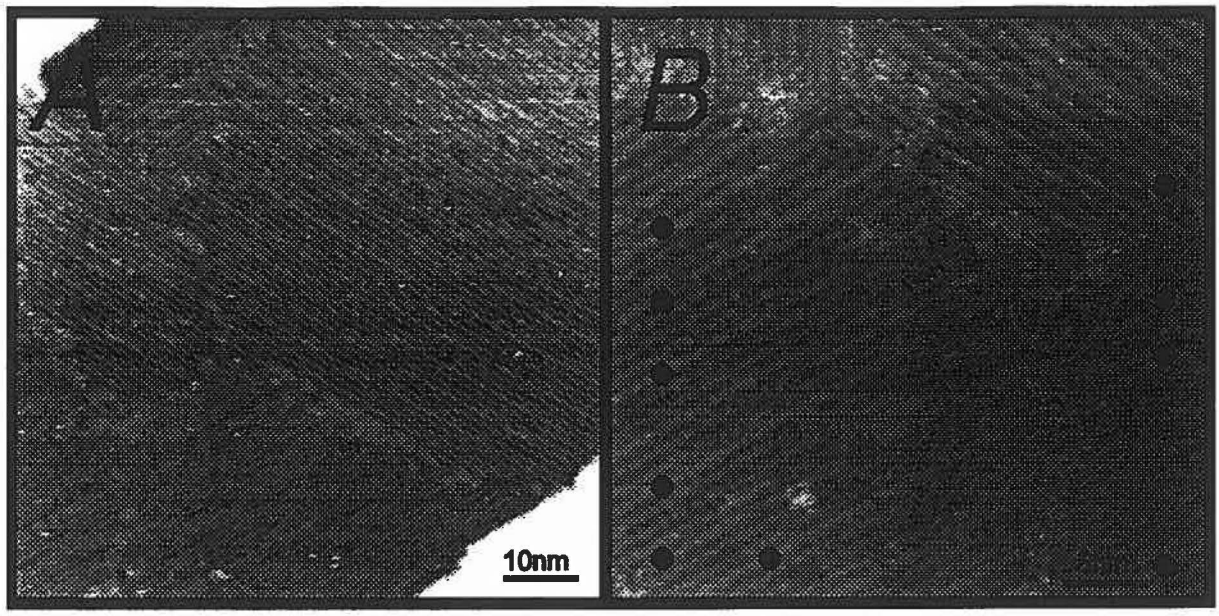


**Figure 3.7** STM images of the fully equilibrated butanethiol monolayer deposited onto the Au/mica substrates. Figure 3.7a shows a 75×75 $nm^2$ region of the surface, while Figure 3.7b shows an expanded 36×36 $nm^2$ view of the striped corrugations that define the individual domains. The black circles (•) identify some of the bright stripes observed in the images.

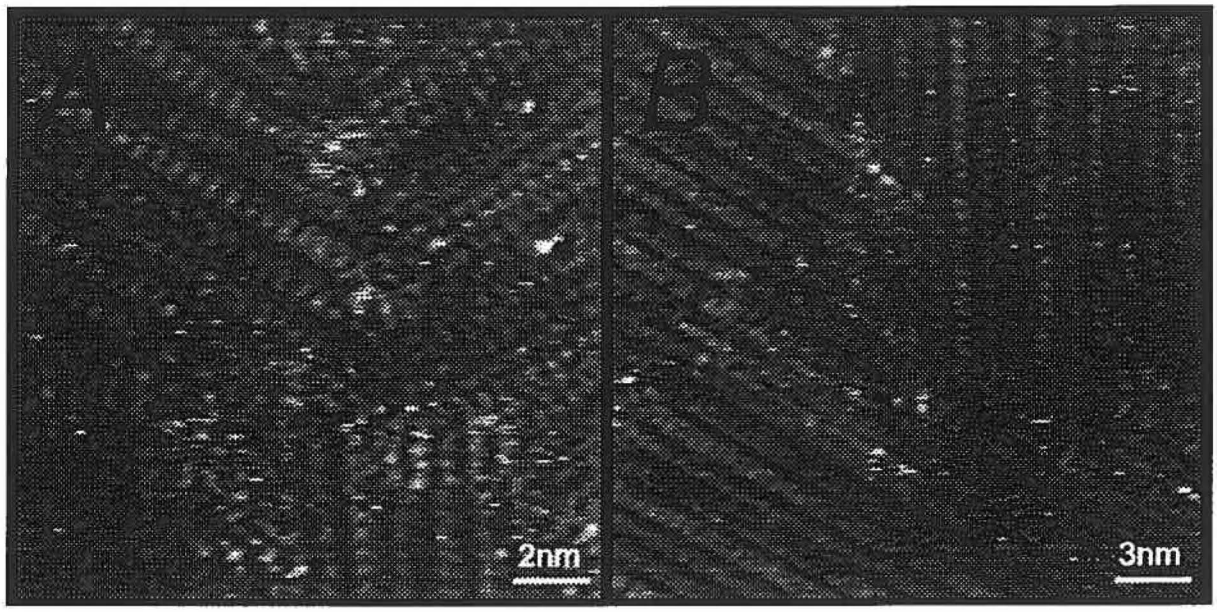


**Figure 3.8** High resolution STM images of individual striped portions of the surface. Figure 3.7a shows a 15×15 $nm^2$ region, while Figure 3.7b shows a 22×22 $nm^2$ surface.

of the freshly-cleaned Au/mica surfaces to the thiol/methanol solutions (i.e., surfaces that are fully equilibrated in solution) leads to a essentially complete elimination of the 'etch pits' introduced by the sulfochromic acid treatment, which will be discussed in next section.

It is interesting to note that within each domain, there are individual stripes that appear systematically brighter than adjacent stripes, presumably due to real differences in elevation. These features are shown more clearly in the expanded view of Figure 3.7b. The bright stripes are approximately 0.2-0.4 Å higher than the more abundant dark stripes. The distribution and relative abundances of the bright and dark striped structures varies across the image, and from sample-to-sample. On average, there are 20-30% bright stripes per domain, and the bright stripes are separated by 1-4 dark stripes; it is unusual to find two adjacent bright stripes. The periodicity of the striped structures (10.3±0.3 Å) appears to be independent of the bright/dark nature of individual stripes (the uncertainty quoted is the statistical uncertainty associated with 75 individually measured profiles, and does not include systematic calibration errors). In virtually all cases observed to date, the bright rows maintain their elevated position across the entire span of the domain, and they rarely survive across boundaries separating parallel domains or the "collision" with an obvious defect of the film; the stripes can therefore be up to 50 nm long for well-prepared films. None of the stripes are affected by repeated imaging of the same region of the surface, and we therefore believe that they are real topographical features of the $C_4$ SAM.

Figure 3.8 shows expanded and higher resolution images of the striped structures. In all cases examined, bright stripes remain bright when imaged at higher resolution. In these images, the individual stripes are in fact pairs of rows within the 10.3 Å stripe width. Parallel to the long axis of these rows, periodic structures with a repeat length of 5.2±0.2 Å is observed. The separation of the rows within a stripe is 4-5 Å , but this is difficult to measure with precision. The most commonly observed pairing has the individual row structures arranged side-by-side, (i.e., perpendicular to the main stripe axis). The row pairing was not successfully resolved when the stripes are aligned perpendicular to the rapid scan direction of the STM (i.e., when they are aligned along the vertical axes of Figure 3.7, 3.8). In some

cases, the vertical stripes appear to have a zig-zag structure, but this is not very reproducible. This poor definition is seen in the lower portion of Figure 3.8a and in the upper right portion of Figure 3.8b. Since the interstripe spacing and elevations appear to be identical regardless of the orientation of the domain with respect to the scan direction (Figure 3.8), we believe that the inability to resolve structure within the vertical stripes is an artifact of the imaging for the $C_4$ SAM surface, and it is probably due to the facility with which the individual chains of the film can be perturbed by the perpendicular passage of the tip (and the associated electric field) over the surface. Nonetheless, the 5.2 Å longitudinal periodicity is frequently observed along these vertical stripes, as shown in Figure 3.8b.

### 3.2.3 Discussion

The primary observation on the surfaces of $C_4$ SAMs is the presence of molecularly resolved structures, as shown in Figure 3.8. The 5.2 Å periodicity along the stripe axes is very similar to the 4.99 Å expected for the intermolecular spacing of the conventional $\sqrt{3}\times\sqrt{3}R30^{o}$ structure usually ascribed to $C_n$/Au(111) SAMs; we therefore believe that the periodic structures observed along this axis of the stripe are the individual methyl terminations of the SAM surface. Poirier *et al.* [Poirier & Tarlov 1994 & 1995] have also observed this characteristic structure along the long axis of their striped structures, and have made the same assignment. This defines the stripe axis to be along the next-nearest neighbour direction of the Au(111) lattice. The 10.3 Å periodicity observed perpendicular to the stripe axes appears to be a fundamental length scale for these films, and therefore, it is assumed to be determined by the periodicity of the Au(111) substrate lattice. In this direction, the gold atoms are arranged in close-packed rows with an interatomic distance of 2.885 Å. The experimental 10.3 Å distance corresponds closely to the 10.1 Å predicted for a 3.5 gold atom repeat length in this direction. The two experimental distances are slightly greater than the theoretical values, suggesting a systematic overestimate of the scanner sensitivity by ~2-4%; this is within

our estimates of the calibration uncertainties. Henceforth the surface structures will be discussed in terms of the 4.99 Å and 10.1 Å distances.

Figure 3.9 presents two structural models that are consistent with the 4.99 Å and 10.1 Å fundamental lengths and relative orientations of the surface structure observed in this study. The spherically shaded sulfur atoms are scaled to an effective diameter of 4.3 Å; this is probably an overestimate, since the sum of the *ab initio* metal-S and S-C bond lengths for the adsorbed thiolates is less than 4 Å [Sellers *et al.* 1993]. The individual rows of molecules are identified as **A** or **B**, according to the distinguishable three-fold hollow sites of the Au(111) surface; all sulfurs along a single vertical row are in equivalent binding sites. The **A** sites are positioned directly over a gold atom in the layer below the adsorption surface (i.e., *hcp* sites), while **B** sites are positioned above voids in this layer (i.e., *fcc* sites). Model I shows four pairs of rows of sulfur atoms arranged on the conventional $\sqrt{3}\times\sqrt{3}R30^{o}$ lattice on the Au(111) substrate; the introduction of a gap between each pair is mandated by the 10.1 Å periodicity in this direction. This gap width is 2.885 Å *less* than the gap created by a full missing row of sulfur atoms (which would correspond to an overall stripe periodicity of 12.98 Å, or 4.5 gold atoms). Each stripe in our experimental data is thus attributed to a pair of thiolate rows, and all thiolates within a stripe must be adsorbed at equivalent **A** or **B** sites. The occasional observation of zig-zag structures in the vertically aligned stripes also supports the $\sqrt{3}\times\sqrt{3}R30^{o}$ internal stripe structure of Model I, but it is clear that this aspect will require further study with higher resolution imaging methods or perhaps lower substrate temperatures to reduce the thermal motion of the alkanethiols. Adjacent stripes can be arranged on the same series of binding sites, as shown by the first, second and third stripes (**AA AA AA**); the basic repeat structure of this surface is a $7\times\sqrt{3}$ superlattice of the underlying Au(111) substrate, containing four molecules in two distinguishable configurations. It is also possible to have all of the adsorbates within a stripe bound into **B**-type sites by displacing an **AA** stripe along the next-nearest-neighbour direction of the Au(111) lattice (i.e., along the stripe axis), as shown in the **AA BB** structure of the third and fourth stripes of Model I. The translation of an entire row from **A** to **B** sites implies a reduction of the binding energy of the thiolates to the surface.

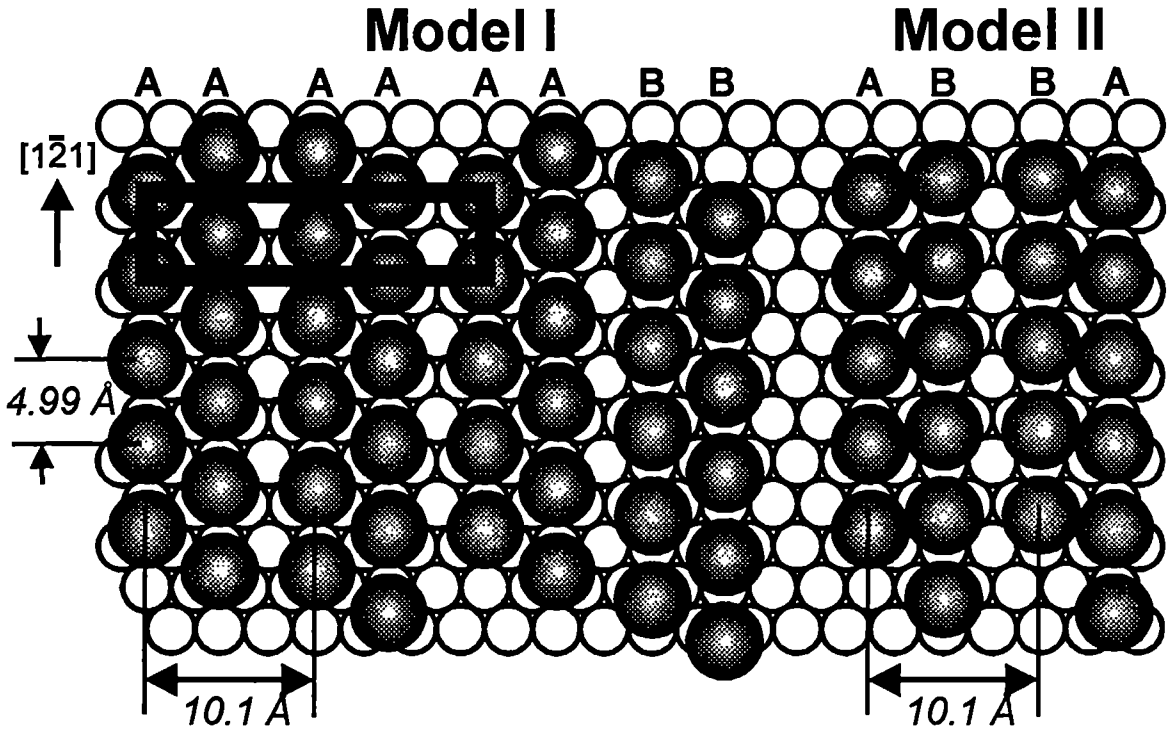


**Figure 3.9** Structural models for the butanethiol SAMs that are compatible with the experimental stripe dimensions and the corrugations due to the methyl terminated surface. Each stripe of Model I is formed from two rows of adsorbed thiolates on the conventional $\sqrt{3}\times\sqrt{3}R30^{o}$ lattice; the $7\times\sqrt{3}$ unit cell is shown. **A** denotes *hcp* adsorption sites that are situated above a gold atom in the second layer of the gold substrate, and **B** denotes the alternative *fcc* sites. Model II is created by translating one row of thiolates along the next-nearest neighbour direction of the substrate, from **A** sites to **B** sites.

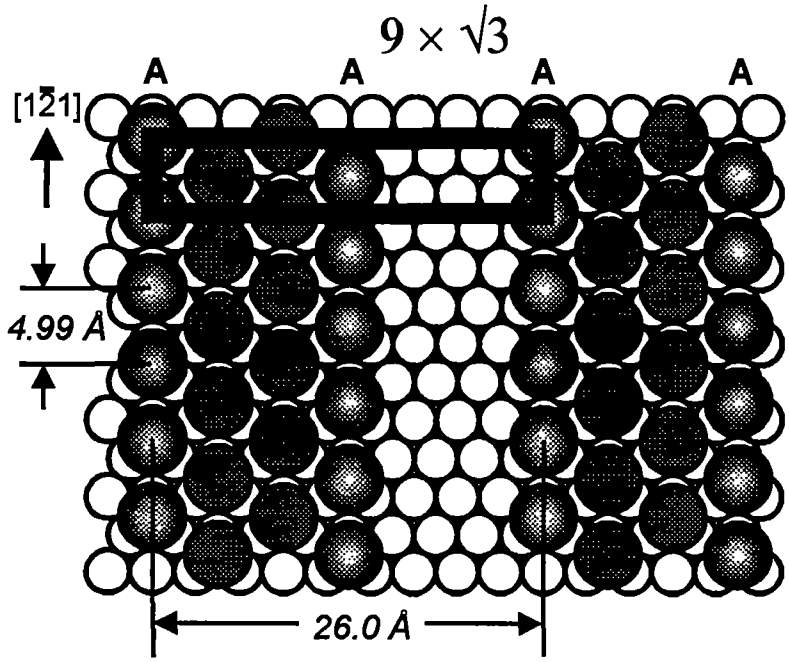


**Figure 3.10** Structural model of the $9\times\sqrt{3}$ structure observed by Poirier *et al.* [Poirier *et al.* 94] for butanethiol monolayers that equilibrate under vacuum conditions. The shaded gray spheres represent the resolved methyl chain terminations in their UHV -STM studies; the solid gray circles show the presumed molecular adsorbates within the pinstripe structure, while the open areas were suspected to be devoid of thiolates.

The *ab initio* calculations of Sellers' *et al.* [Sellers 1993, Sellers *et al.* 1993] have shown that the ~44 kcal/mole binding energy of individual methylthiolates to the **A** sites of the Au(111) lattice is due in part to the overlap of the sulfur atom's σ orbitals with the gold atom directly below the sulfur in the second layer of the substrate. Interestingly, the influence of the second layer is less important in the case of thiols adsorbed onto the **A** sites of Ag(111) surfaces; interactions with the second layer of the substrate contributes to the significantly shorter sulfur-surface bond lengths [Sellers *et al.* 1993] found with $CH_3S$-Au(111) than with $CH_3S$-Ag(111) (1.905 Å *vs.* 2.332 Å, respectively) and with HS-Au(111) *vs.* HS-Ag(111) (1.978 Å *vs.* 2.337 Å, respectively). We therefore surmise that a weaker **B**-site binding energy would cause these adsorbates to be positioned slightly farther from the plane of the gold substrate than those at **A** sites, and it may also cause an asymmetry in the electronic structure of the adsorbed sulfur atoms. The experimental height difference of the bright and dark stripes (0.2-0.4 Å) would be a reasonable consequence of this change in the S-Au(111) bonding. STM imaging is sensitive to both the height and the electronic structure of the bonding, and we believe that this may provide a mechanism for the observed bright and dark stripes in the data presented herein. As noted above, the bright stripes are less abundant than the dark stripes, as would be expected for adsorption at the less-energetically favorable **B** sites. Furthermore, this structure is consistent with the observation that stripes usually extend across entire domains (but no further) without changing their bright/dark identity, since the **A** and **B** site definitions are defined by the substrate periodicity that extends well beyond the domain regions of the SAM structures. At the disordered interface between domains that have nucleated and grown from different points on the substrate, the stripes can lose their **A** or **B** registry with the substrate, even if the adjacent domain is aligned along the same direction of the surface.

One observation that is not addressed in Model I is the apparent pairing of adjacent methyl groups within a stripe. In view of the lateral degrees of freedom that are available to the individual $C_4$ chains at 300 K (no thiolate has six closely-packed neighbors in a 10.1 Å stripe model), the observed row pairing probably reflects the conformations of the methyl

terminations, and is not therefore directly related to the spatial distribution of the underlying sulfur lattice. The lack of direct correlations between the methyl terminations and the S lattice is supported by the inability to resolve the intrastripe pairing structure for certain orientations of the stripes with respect to the raster direction. Nonetheless, we present in Model II (Figure 3.9) an alternative structural model that could rationalize the observed pairing structures. In this model, the two sulfur atoms lying perpendicular to the long axis of the stripe are in non-equivalent binding sites; this could be achieved by translating one row of a stripe along the stripe direction until it is in registry with the **B** sites. This produces a more rectangular structural unit than that of Model I, with the consequence that the two rows of a stripe are necessarily in non-equivalent binding sites. We believe, however, that the observation of bright and dark stripes is more significant and reproducible than the apparent pairing of the relatively unconstrained methyl terminations at ambient temperatures; accordingly, we favour the interpretation presented as Model I.

These structural models can best be compared to the $p\times\sqrt{3}$ structures seen by Poirier *et al.* [Poirier *et al.* 1994, Poirier & Tarlov 1995] in their UHV-STM study of the crystallization of disordered phases into ordered assemblies. Figure 3.10 shows the $9\times\sqrt{3}$ structure shown in their high resolution images [Poirier *et al.* 1994]; the sulfur atoms marked as gray spheres were individually resolved in their experiments, while the sulfur atoms shown as solid gray were not resolved, but were presumed to be present on the basis of the measured heights between the methyl terminated rows. The open areas 'may be devoid of molecules' [Poirier *et al.* 1994]. Although both the UHV-STM and the results presented herein show well-oriented rows of methyl-terminated chains with the 4.99 Å separation, the structures perpendicular to this axis are clearly different. If the open areas of the $9\times\sqrt{3}$ structure are in fact devoid of molecules, the overall coverage is ~66% of the coverage for a full $\sqrt{3}\times\sqrt{3}R30^{O}$ structure; in the less likely case that the sulfur atoms marked in gray are also missing, the surface coverage drops to 33% of a full monolayer. The $5\sqrt{3}\times\sqrt{3}R30^{O}$ and $4\sqrt{3}\times\sqrt{3}R30^{O}$ models proposed by Dubois *et al.* [Dubois *et al.* 1993] for their vacuum-prepared $C_4$ SAMs have 80% and 75%

coverages, respectively. In contrast, the coverages for our Model I and II structures are each 1986%.

The observation of relatively large surface coverages for $C_4$ SAMs in this work is supported by the recent IR-RAS studies of fully equilibrated sub-monolayer $C_4$ films in our lab [Truong & Rowntree], which found that the $C_4$ films grow by island formation. The optical absorbance of the $r^+$ methyl symmetric stretch (2876 $cm^{-1}$) is linearly related to the total quantity of thiol in the deposition solution, which is believed to be the quantity adsorbed in the fully equilibrated sub-monolayer films. This behaviour is shown in Figure 3.11; 1.0 monolayer corresponds to the adsorption of a full $\sqrt{3}\times\sqrt{3}R30^o$ SAM ($4.64\times10^{14}$ /$cm^2$). The IR-RAS data for $C_4$ SAMs produced by extended exposure of Au/mica substrates to thiol/methanol solutions containing one or more monolayers of dissolved butanethiol are indistinguishable, and the intensities are invariant to within ±5%; the intensity of the $r^+$ band for these saturated monolayer spectra is shown as the horizontal line of Figure 3.11 (1.9±0.1 milliabsorbance units). The sub-monolayer intensities converge to the maximum intensities at

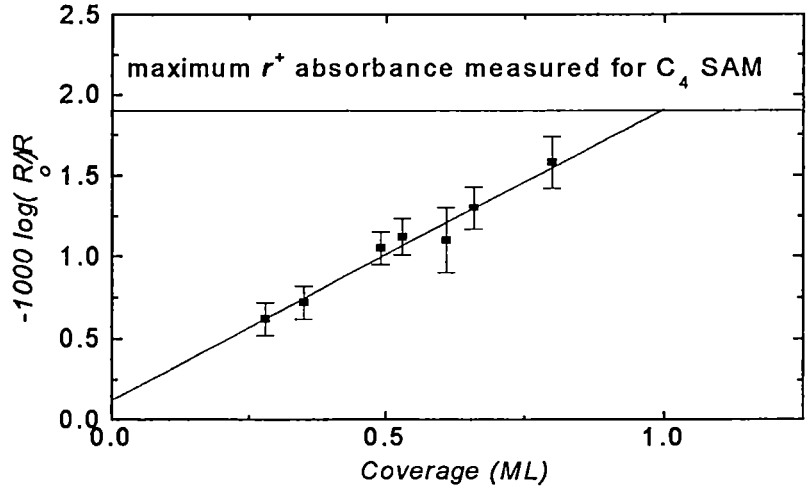


**Figure 3.11** Trends in the optical absorbance of the $r^+$ symmetric stretch (2876 $cm^{-1}$) of the terminal methyl group of fully equilibrated $C_4$ thiol films adsorbed on Au/mica substrates, as a function of the total quantity of butanethiol available for adsorption in solution. R and $R_0$ are the infrared reflectivities of the Au/mica surface with and without the adsorbed SAM, respectively. Full monolayer coverage is defined by the $\sqrt{3}\times\sqrt{3}R30^o$ structure ($4.64\times10^{14}$ molecules/$cm^2$). Full details of this work are presented elsewhere [Truong & Rowntree].

coverages that correspond closely to that calculated for the full $\sqrt{3}\times\sqrt{3}R30^{o}$ monolayer. This would not be the case if the thiols in solution could not adsorb *& stay adsorbed* in the large open regions of the $9\times\sqrt{3}$ structure. If large voids in the SAM were stable while exposed to thiolate solutions, the optical absorbance would be anticipated to approach the limiting value at surface coverages 33%-66% *below* that of the full $\sqrt{3}\times\sqrt{3}R30^{o}$ coverage (i.e., the slope would be greater), depending on the identification of the gray regions within the pinstripes of Figure 3.10. It should be noted that if there was an equilibrium between adsorbed and dissolved thiols (such that significant quantities of dissolved thiols would remain in solution for the sub-monolayer film preparations) the sub-monolayer band intensities would approach the full-monolayer intensities only with solutions containing significantly *more* than 1.0 monolayer of thiol (i.e., the slope would be less).

Although the Poirier studies have the advantage of using single crystal Au(111) surfaces in place of our Au/mica films, each of the full $C_4$ SAMs used in this work has been deposited from relatively concentrated alcohol-based solutions in essentially the same manner. The central difference between the sample preparation in their STM studies and those reported herein appear to be that our $C_4$ films are equilibrated while exposed to the thiol/methanol solutions, while their samples were equilibrated under UHV conditions (indeed, the purpose of their studies was to observe *in-situ* the dynamics of the equilibration process by STM). Similarly, the $C_4$ SAMs examined in the LEED experiments of Dubois *et al.* [Dubois *et al.* 1993] were prepared by dosing Au(111) surfaces under vacuum conditions, producing coverages intermediate between those of Poirier *et al.* and this work. These authors also found that short-chain adsorbates (e.g., $C_1$ and $C_2$) required extended dosing due to the lower sticking probability, and this prepared full $\sqrt{3}\times\sqrt{3}R30^{o}$ monolayer structures. These results suggest that crystallization of the SAM structure under vacuum conditions may lead to significantly more irreversible desorption than is the case for equilibration while exposed to a solvent. The mechanism for this difference is not clear, but it may be due to the ability of desorbed molecules to return to the surface if exposed to the solution phase (or if additional molecules can adsorb in the case of extended gas-phase dosing), and thus recuperate the

losses due to initial desorption. This would also suggest that the choice of solvents may be crucial in determining the ultimate structural characteristics of the adsorbed film. These findings may have important consequences for the preparation of these films prior to characterization such as sub-monolayers, and for the use of these films in electronic or sensor applications.

We have successfully resolved the molecular structure of butanethiol monolayers on Au(111) surfaces. The surface topography of such films depends on the tunneling resistance, i.e., tip-sample separation. As the applied bias voltage only varied in a small region (~0.1-0.5 V) in our experiments, this usually shows as the dependence to the tunneling current. The STM images obtained with low current (~20-40 pA) yielded reproducible molecular resolution, while higher current (~0.3 nA) conditions only revealed such molecular structures occasionally and in poor quality. Along with similar observation reported by Shönenberger *et al.* [Shönenberger *et al.* 1994], the high-resistance tunneling junction was found to be the optimized conditions for imaging such thin organic monolayers at high resolution. There are several reasons for us to believe that the observed molecular structures reflect the variance of the methyl terminations and not the sulfur lattices of the $C_4$ chain under such conditions. First is the apparent elevation of the disordered boundaries between the individual ordered domains. Earlier studies by infrared spectroscopy [Porter *et al.* 1987, Truong & Rowntree] and optical ellipsometry, electrochemsitry [Porter *et al.* 1987] have shown that SAM consists of fully extended molecules in all trans transformation and the fully-equilibrium $C_4$ SAM molecular orientation is tilted ~30-35° away from the surface normal. Since the molecules are tilted to approximately same orientations in each ordered domains, the methyl terminations of $C_4$ chain from different domains will conflict with each others and thus cause the disordered and elevated interfacial boundaries. No obvious reason was found for this phenomena when the sulfur lattices were being imaged. On the contrary, if the tunneling current was dominated by the direct interaction between the tip and the sulfur lattice, it is probable that the introduction for these disordered regions near the sulfur would lead to an decreased transmission probability, and apparently lower topographical features. The second evidence is

the observation of different superlattice of a basic $\sqrt{3}\times\sqrt{3}R30^{o}$ structure for *n*-alkanethiol monolayers on Au(111) by using a low tunneling current STM (10-30 pA) [Camillone *et al.* 1994, Delamarche *et al.* 1994, Poirier & Tarlov 1994, Shönenberger *et al.* 1995]. Since all the *n*-alkanthiol molecules bind to equivalent Au lattice sites in $\sqrt{3}\times\sqrt{3}R30^{o}$ structure, the height variance in the unit cells are more likely caused by some variations in molecular orientations [Poirier & Tarlov 1994]. Meantime, the STM images obtained with high tunneling current (i.e., low-resistance tunneling junction, Bias 0.05-0.3 V, Current 0.2-20 nA) revealed the basic $\sqrt{3}\times\sqrt{3}R30^{o}$ structures only [Widrig *et al.* 1991, Kim *et al.* 1992]. It seems that the STM is imaging the sulfur lattices under such tunneling conditions because the tip-sample separation is very small and the tip may penetrate into the films.

## 3.3 Self-Assembled Butanethiol Sub-Monolayers on Gold

After successfully molecular imaging of butanethiol monolayer films on gold substrates, we have found that the film preparation technique and tunneling condition have a large impact on the resulting STM images. The $C_4$ SAMs fully-equilibrated in solutions show highly structural molecular ordering and STM images of such films yields molecular resolution under high-resistance tunneling junctions. Such molecular structures are fairly stable under clean ambient conditions and repeated imaging; no evidence was found for tip displacement of these structures under the optimized tunneling conditions during scanning in our experiments. This section illustrates our results for imaging butanethiol *sub-monolayer* films by applying these techniques learned from the previous work [Kang *et al.*].

Figure 3.12a is an image of 42% fully equilibrated sub-monolayer $C_4$ films, where the coverage is calculated based on the full $\sqrt{3}\times\sqrt{3}R30^{o}$ structure. As expected, the island formations of the $C_4$ SAM are clearly shown on all the terraces. These islands are connected to each other on the terraces, with ~15-25 nm lateral dimensions. No islands have been observed to be connected across surface defects (such as atomic steps). Figure 3.12b is a higher resolution image of 25% of sub-monolayer film; the striped structures are clearly shown within the island formations. The disordered boundaries were also observed on edges of the islands. This observation confirms the assignment that these organic islands are composed of $C_4$ molecules, while the darker part of the surface is devoid of molecules. The island coverage can be calculated from the images of the sub-monolayer films; the comparison of this value to the indicated coverage may provide some useful information to verify the SAM structural models. For the 25% and 42% sub-monolayer films, the organic island coverages, i.e., the measured SAM coverages based on the STM images, are 28.5±5% and 48.5±5% respectively. The factor differentiating these values from the calculated coverages is 0. 87±0.01. This factor is consistent to the 86% coverage of a full $\sqrt{3}\times\sqrt{3}R30^{o}$ structure for $C_4$ monolayer films with the structural models we proposed in last section.

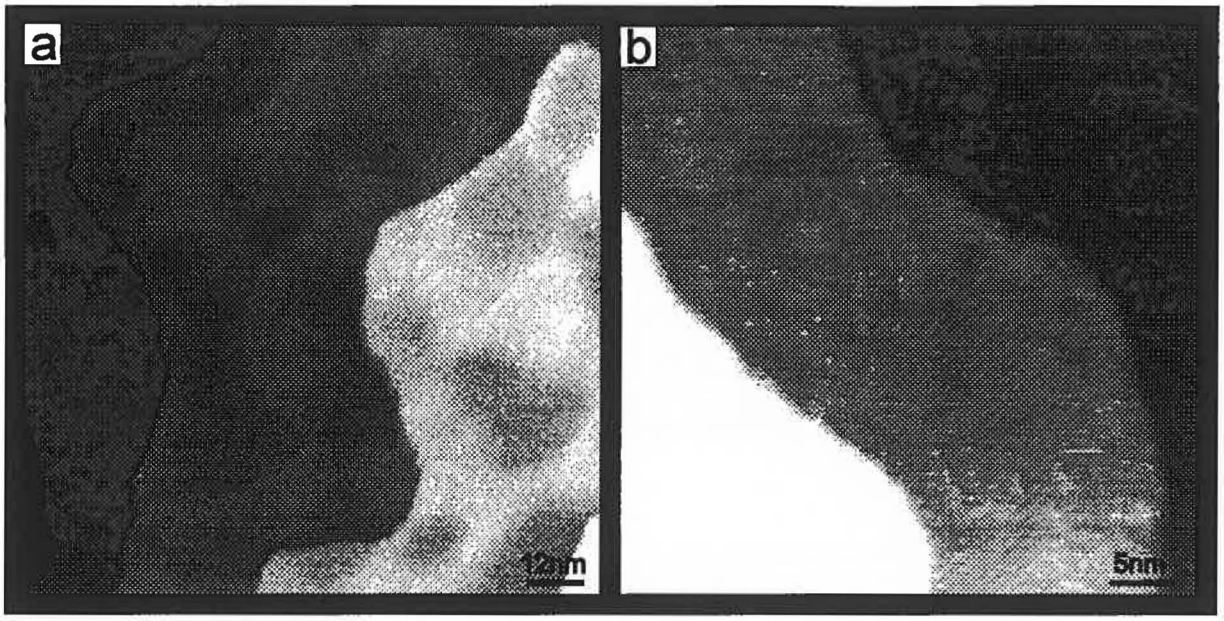


**Figure 3.12** Island-like formation of fully equilibrated butanethiols sub-monolayer on Au/mica surfaces. The coverage is calculated as (a) 42%, (b) 25% based on the conventional $\sqrt{3}\times\sqrt{3}R30^{o}$ lattice structure of $C_4$ SAM. Scan size: (a) 120×120 $nm^2$, (b) 45×45 $nm^2$.

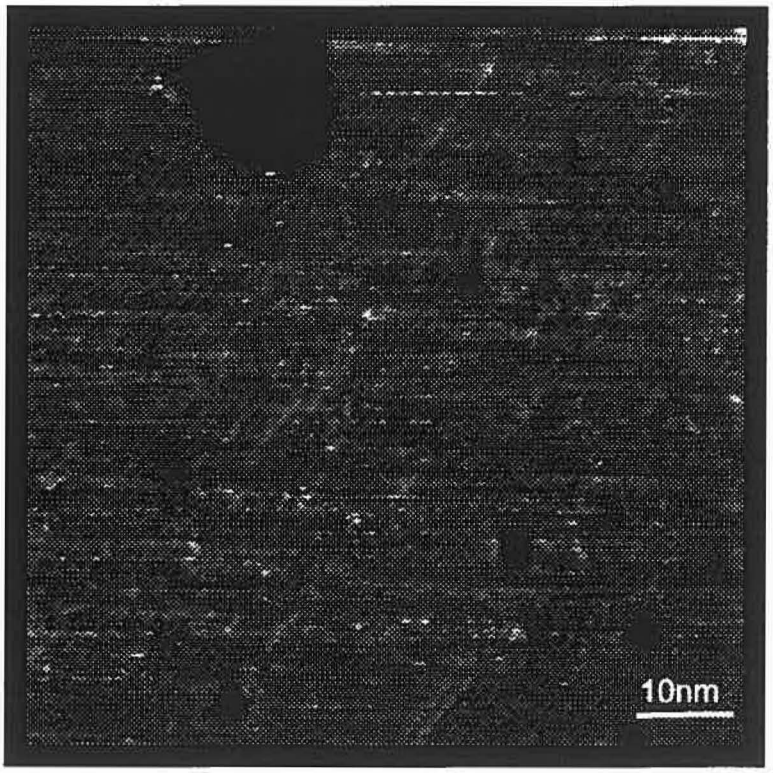


**Figure 3.13** A high resolution STM image of 76% $C_4$ films with residual one-atom deep holes. The striped structures are the same as found with full monolayer films. Scan size: 75×75 $nm^2$.

A higher resolution image of $C_4$ sub-monolayer films is given in Figure 3.13, where the coverage is indicated as 76% of the full monolayer based on a full $\sqrt{3}\times\sqrt{3}R30^o$ structure. The striped structures are organized in differently oriented domains, with the elevated interfacial boundaries between the individual domains, as observed in full-monolayer films. The difference is that now there are some residual near-circular atomic pits on the surface, with diameter ~2-5 nm. Striped structures were also observed in the larger holes, while no detailed information in smaller holes is available because of the finite tip radius. This also makes the precise measurement of organic island coverage impossible in such high coverage sub-monolayer films.

Figure 3.14 is a large scale image of $C_4$ 42% sub-monolayer film. As in Figure 3.12, the organic island formations are clearly shown on all the terraces in this image. One aspect addressed in this image is that of the surface defects; many of one-atom-deep holes appear on the surface, with lateral dimensions from a few nanometers to ~60 nanometers. These holes are mostly distributed near the step edges; the step edges are more convoluted when compared to untreated gold films. The curvatures of most step edges become smaller or even negative. The organic islands structures of $C_4$ SAM are also observed inside the bigger holes. Interestingly, these holes are systematically surrounded by islands structures. Similar defects were systematically observed in the $C_4$ sub-monolayer films we examined, but never shown on untreated gold surface. The residual holes in 25% sub-monolayer films have lateral dimensions ~15-30 nm; while large scale images of 76% films also showed the convoluted step edges. But in the full monolayer films, no etching pits or convoluted step edges have been observed.

Based on above observations, it could be concluded that the residual surface pitting exists on the surface if the thiol solution contains less than one equivalent monolayer. The fully equilibriated formation of complete $C_4$ monolayer films leads to an essentially complete elimination of the "etch pits" introduced either by sulfochromic acid treatment or by thiol adsorption. In the absence of direct observations of the surface evolution over extended

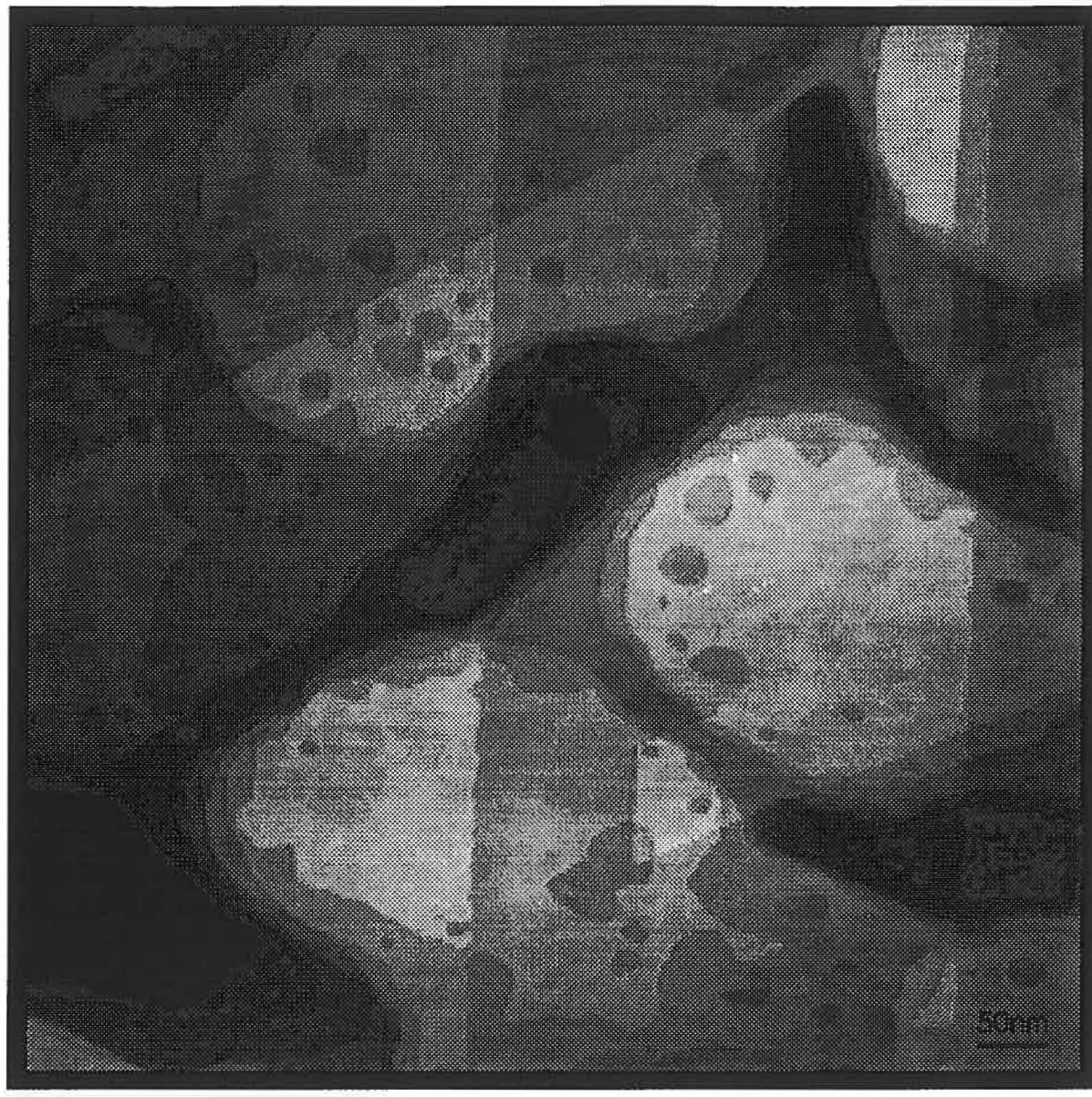

**Figure 3.14** A 750×750 $nm^2$ image of 42% butanethiols sub-monolayer films. The island formations could be seen on all terraces.

periods of time, we can only speculate on the mechanism of the pit evolution, but it is clear that the lateral diffusion of gold

atoms is required to effect such a transformation. · We believe that the evolution of the pit-type defects during film formation is closely related to the 'Ostwald ripening' of large pits at the expense of small pits reported under UHV conditions by Poirier and Tarlov [Poirier & Tarlov 1995]; the pits in their studies were created by the adsorption of the thiols onto the gold substrates. Under their conditions of fixed (and limited) adsorbate availability, they observed that the topology of the gold substrate ceased to evolve once the organic monolayer had 'crystallized' into its well-defined striped phase, which is consistent to that found for surfaces exposed to sub-monolayer thiol-containing solutions. The curvature's change of the step edges on the sub-monolayer SAM can be also explained by this lateral diffusion of gold atoms, which stops while the SAM has been fully equilibrated, i.e., crystallized. It is obvious that the molecular interactions on the surface act as the key factor of this diffusion process. The complete absence of pits in the full-monolayer fully-equilibrated images presented herein may be the consequence of our surfaces being equilibrated with essentially unlimited quantities of thiols in solution, which can produce significantly greater thiol coverages than those equilibrated under UHV conditions.

One observation that is not addressed above is the vertical dimension of the organic island structures. These structures have ~0.5-1.0 Å height elevations above the surrounding surface in average for the sub-monolayer films. It has been noticed in last section that the internal molecular structures reflect the variance of the methyl terminations but not the sulfur lattices of the $C_4$ chain under the optimized tunneling condition (Bias 0.1-0.5 V, Current 25-40 pA). Thus the height variance on the sub-monolayer films could be considered as the thickness of the $C_4$ SAM measured by STM. As mentioned before, the butanethiol molecules in the fully-equilibrium $C_4$ SAM are fully extended with molecular orientation ~30-35° away from the surface normal [Porter *et al.* 1987, Truong & Rowntree]. If an average tilt of 32° is introduced to that model, the physical thickness of the $C_4$ monolayer can be estimated as ~8.0 Å from tabulations of covalent and van de Waal radii based on this model [Porter *et al.* 1987].

This physical value is significantly different from the measured thickness because STM is sensitive to the elastic and electrical properties of the surface. The height measured by STM reflects the difference of the LDOS at Fermi level between Au(111) and $C_4$ SAM/Au surfaces. The contribution of butanethiol molecule to the LDOS may be related to the change of the molecular orbitals of the alkane SAM due to the Au-S bond and molecular interactions and does not necessarily have to correspond to its physical height. Nonetheless it is difficult to explain the details of these data because the tunneling mechanism for imaging such ostensibly "insulating" organic films remains an open question. In the case of biological adsorbates (e.g. DNA) imaging, this issue becomes more complicated because of the relatively larger molecular dimensions and the complex structure of biological specimen.

## 3.4 Imaging of DNA Adsorbates

Until now, the monolayer and sub-monolayer films of $C_4$ SAM on Au(111) surfaces have been successfully imaged in molecular resolution by STM under the optimized tunneling conditions. These structures did not show any displacement by the tip under repeat scanning. After the butanethiol molecules were chemisorbed to the Au(111) surface via Au-S bonds and equilibrated in solutions, surfaces with sub-monolayer films changed their morphology with atomic pits and convoluted step edges. Such modifications are permanent and stable during scanning. These STM results (including SAM coverage) are consistent with the IR-RAS spectroscopic results from our laboratory. This section gives the results of DNA adsorbate imaging using the techniques and knowledge acquired in the previous studies.

Figure 3.15 gives an image of ΦX-174 RF I plasmid on HOPG surface. Two nearly parallel stripes extend across the surface, with clearly resolved helical structures. Each stripe is ~2 nm wide and has longitudinal periodicity 3.6±0.2 nm in average; they are ~3.5 nm apart from center to center. These values are very close to the dimensions of double-stranded B-form DNA, which has 2nm radius and 3.4 nm per turn. Large scale images show that this helical structures with >1.5 μm extended length, where this long chain plasmid is ~1.8 μm circumference in B-form. This dimension was not precisely measured because of the limited scanning range, which is due to the limited linearity range of the piezo elements in the scan tube. Therefore we believe the two stripes are part of a circular DNA molecule, which was folded and aligned probably by scanning. The height of the two stripes was ~1-2 nm above the substrate. This value is close to 2 nm, the already known radial dimension of the B-form DNA molecule [Alberts *et al.* 1989, Saenger 1984]. The variance is probably due to the spatial interactions between segments of the molecule and substrate, which may contribute to the stability of the molecule under scanning. Another feature in Figure 3.13 is the periodical structure in the regions of the image "below" the DNA, which has the same periodicity as the helical structures, along with ~1 nm above the substrate plane. This structure continues

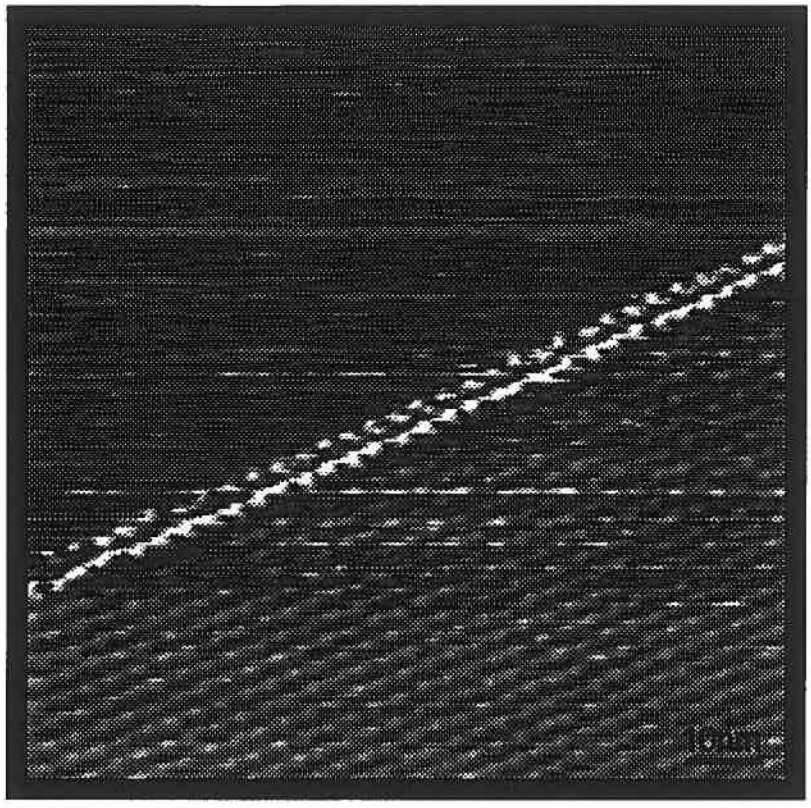

**Figure 3.15** An 100×100 $nm^2$ image of ΦX-174 RF I DNA deposited on a graphite substrate. The helical structures of the DNA are clearly presented.


**Figure 3.16** A 450×450 $nm^2$ image of ΦX-174 RF I DNA deposited on a freshly prepared gold surface.

below the plasmid while we traced this molecule several hundred nanometers across the surface until another defect structure. It is not clear what this structure is, but it may be an artifact on the polycrystalline graphite introduced by tunneling junction change due to the existence of the folded molecule or small particles of graphite on the tip.

Figure 3.16 is a lower resolution image of ΦX-174 RF I plasmid deposited on a freshly prepared Au/mica surface by the second deposition method, i.e., keeping the sample undisturbed for 6-12 hours at +4 °C in an environment with 100% relative humidity after a 5-10 μl drop of ~40 μg/ml aqueous solutions directly deposited onto the substrates. Five objects are clearly shown on the surface, where three of them extend across the Au(111) steps. These objects are very stable under repeat imaging. Similar helical structure also appeared on all these objects in this image with different dimensions: each turn is ~8-30 nm in longitudinal direction. It is very obvious that these objects are in different sizes; they are ~100-150 nm long, ~5-35 nm wide and ~2-9 nm high. But the unusual structure similarities of these objects suggest that they are probably produced by "multiple tip" imaging artifacts from one real structure. This also suggests that the DNA molecules tend to be folded together and this folded structure is probably a more stable form than their extended counterpart, especially if the molecules were partially dehydrated during the deposition. No sub-molecular details were obtained, although these molecules were stable for at least 4 hours during scanning.

Figure 3.17a is a low-quality image of 123-ladder DNA molecules adsorbed side-by-side on a ***S*** acid etched gold substrate near the edge of the topmost terrace surface. The atomic holes of the gold surface created by ***S*** etching are clearly shown on this image; these holes may increase the affinity of the substrate to the physisorbed molecules by minor deformations. The similar volumes of these two objects suggest similar compositions, while in this image the object on the right (marked by solid arrow) appears to be divided into two fragments of ~20 nm length each in this image. The image acquired immediately after this image (Figure 3.17b) shows the object on the left was also being broken at the similar site during the scanning process. It is also noticed in this figure that the atomic holes created by ***S*** acid etching are

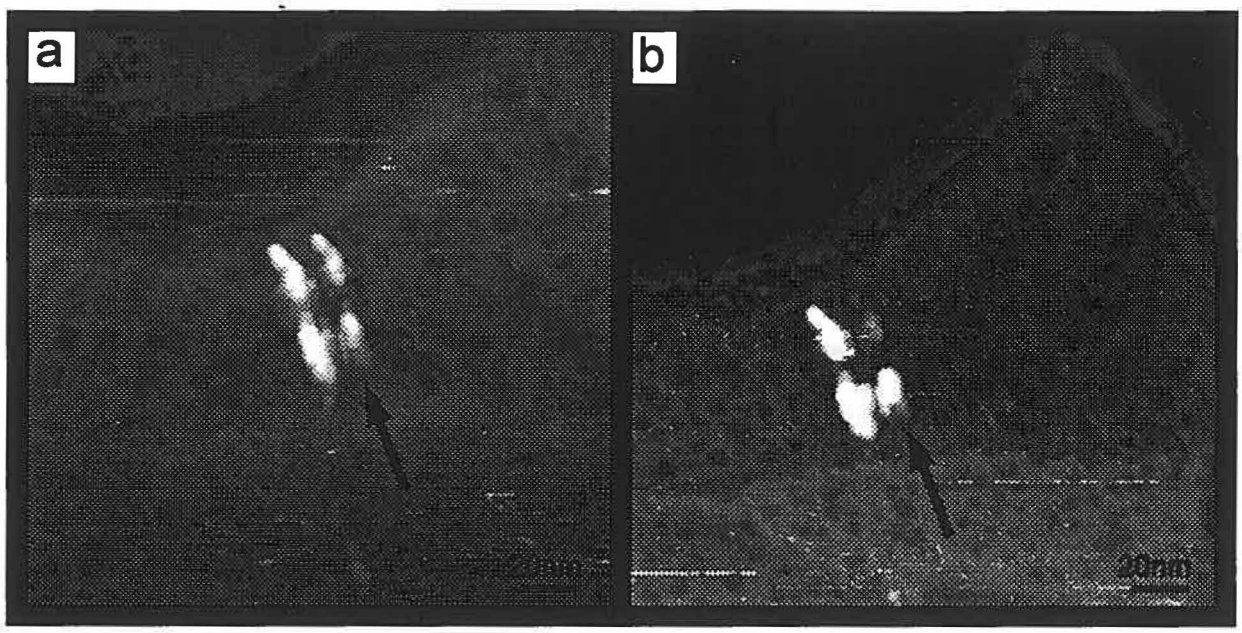


**Figure 3.17** Images of two 123-ladder DNA deposited on a ***S*** acid treated Au/mica substrate. The molecules appear to be "broken" near the mid-points by scanning. Bias: 0.5 V, Current 30 pA, Scan size: 200×200 $nm^2$.

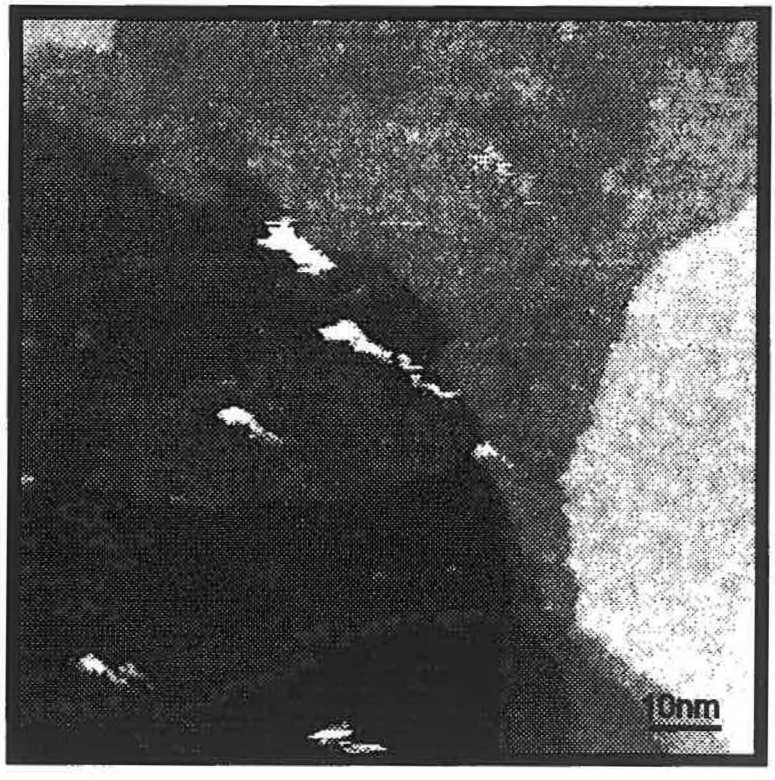


**Figure 3.18** Image of thiolated $A_{50}$ oligo-nucleotide segments adsorbed onto an untreated gold substrate; each ~15 nm "white" linear segment is believed to be an individual molecule. Size: 100×100 $nm^2$.

clearly shown in the region between these fragments, which confirms that the lower height between fragments is not merely a loss of image contrast but real topographical structures. Thus we have reason to believe that these two object on the right may have been a single 123 ladder particle at the beginning of the experiment; and that it was broken into two pieces prior to acquiring the first image. The tunneling condition applied for these two images is 1.0 V bias, 30 pA tunneling current, which corresponds ~33GΩ tunneling resistance. The multiple double strands breaks (dbs) happened so quickly under such high impedance tunneling junction, suggests that there may be a "hot site" sensitive to radiation damages near the middle of the molecule. Unfortunately, we have not been able to reproducibly resolve sub-molecular structures for this adsorbate, and the observation of the molecular scission has not been repeated.

Figure 3.18 is an image of thiolated $A_{50}$ oligonucleotide sequence on untreated Au supports because the molecular length of ~16 nm is too similar to the typical size of the etch holes to allow the use of the higher contrast substrates. This image shows a series of structures, each of which is believed to be a single $A_{50}$ strand. No analogous structures have ever been observed on the bare gold substrates of images obtained using oligo-free solvents. Large numbers of these strands were reproducibly observed by using 5 μl of a 10 μg/ml solution ( containing ~25 monolayers of oligonucleotide sequences), suggesting that the covalent bonding facilitates adsorbate stabilization in the region accessible to the STM probe. Repetitive imaging of the same molecule at high magnification tends to collapse the oligo strand into a hemi-spherical particle, showing that increasing bonding to the substrate would be advantageous to minimize such self-affinity.

In our experiments, the second sample deposition method yields slightly higher quality of the images. This is probably due to the extended period of DNA molecules to attach on the substrates. Most importantly, it is also found that the *observable coverage* is only weakly correlated to the quantity of DNA deposited; we frequently applied the equivalent of 5-15 complete layers in order to increase the possibility of observing isolated molecules. As found with butanethiol SAM imaging, the image stability is dependent upon the bias polarity, with

the highest quality images obtained when the tunneling takes place with electrons passing from the probe tip into the sample/substrate.

New deposition techniques have also been applied in our experiments. The first is the surface modification by immersing the freshly prepared evaporated gold films (without acid treatment) into 5 mM 2-dimethylaminothiol solutions ( containing in excess of 1 monolayer of DNA molecules) for 12 hours. It was suggested that the pendant cationic groups on this chemically modified surfaces could bind DNA [Bottomley *et al.* 1992, Allison *et al.* 1992] by the fact that DNA molecules are negatively charged [Alberts *et al.* 1989]. While previous reports of uncoated DNA images showed lower resolution and even negative contrast, it was reported that DNA molecules could be reliably and reproducibly imaged by STM and AFM with this technique [Bottomley *et al.* 1992, Allison *et al.* 1992]. After the substrate modification, the gold terraces are still clearly seen, along with one atom deep holes (Figure 3.19). These pit defects were probably introduced by the surface thiolation process, as introduced by the alkanethiol deposition process on Au surface [McDermott *et al.* 1995, Poirier & Tarlov 1995]. The DNA deposition were performed with diluted ΦX-174 RF I plasmid solutions while the Au/mica film were incubated in the solutions for 3 hours at +4°C with the gold side down. The quantity of the plasmid in solutions ranges from sub-monolayer to several monolayer. The result images are not promising; the tip crashed very often while approaching the tunneling junction, and even after the successful approach the first few images were often very noisy, with unstable and indistinguishable topography. This phenomena suggests that there was a non-conductive adsorbate introduced onto the surface, thus preventing the electrons from tunneling through the barrier. The DNA molecules are probably folded together and form thick, non-conducting layers on the substrate. This layer could be removed by the tip while scanning, such that the gold terraces were exposed again after few images. Small aggregates (about few nanometers across and 1 nm high) near the surface defects were often observed on the surface after 2-8 scannings under normal tunneling conditions (0.5 V, 30 pA), which were not reproducible for the repeat imaging. These aggregates may be the broken segments of the plasmid molecule or particles of ammonium

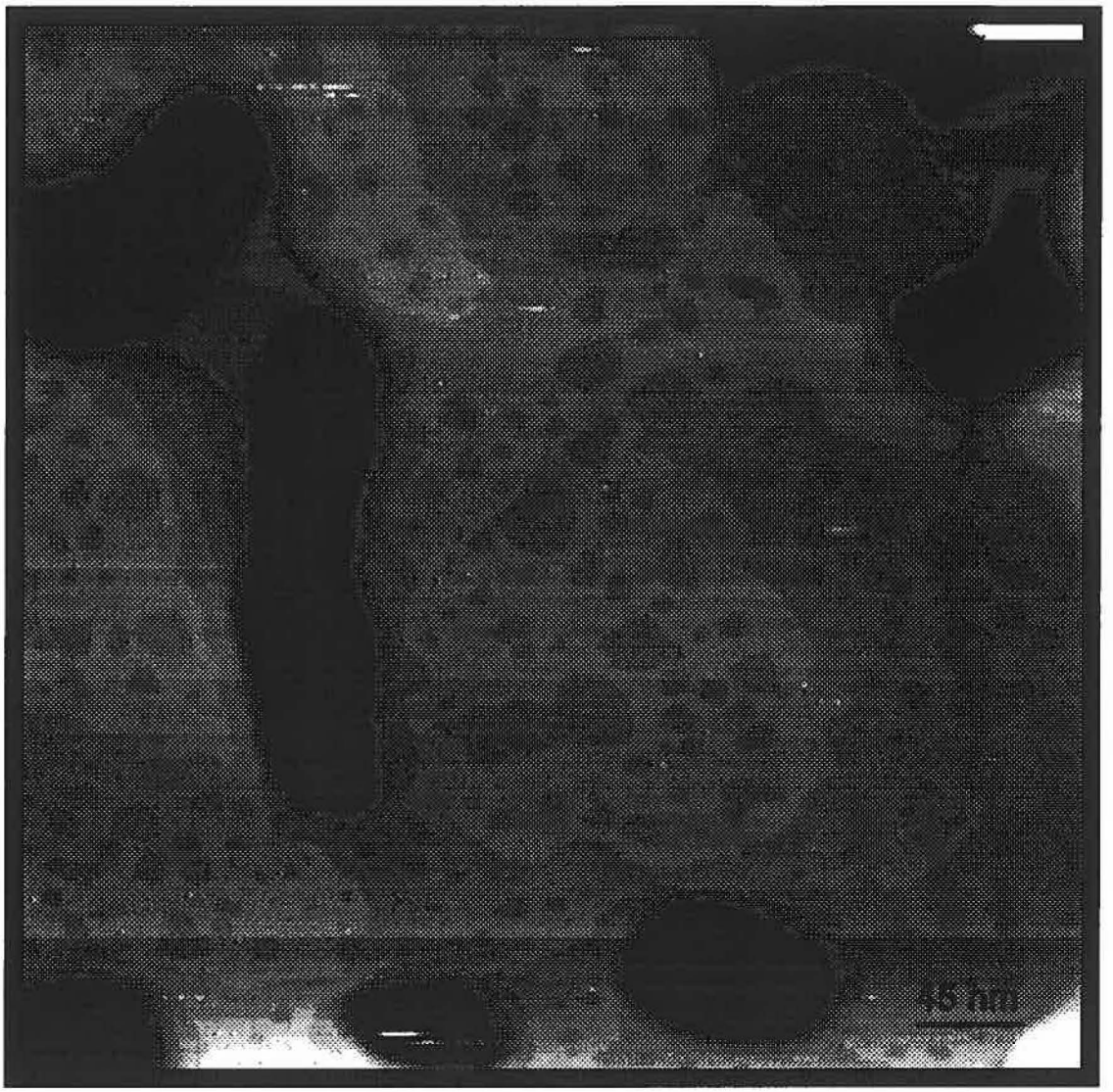


**Figure 3.19** A 450×450 $nm^2$ image of 2- dimethylaminothiol treated Au/mica films. The atomic depressions are similar to those found on $C_n$ SAM/Au surfaces.

acetate in DNA solutions. Molecular combing techniques were also performed on the chemical modified gold substrates, which was supposed to make the DNA distribution more uniformly. Nonetheless no isolated molecules have been observed, even when the solutions containing the equivalent of ~5-10 complete layers were used.

We have reported our efforts to image DNA adsorbates with different substrate and sample preparation; it was found that the DNA molecules tend to be folded or aggregated together. These aggregates may be formed by dehydration during sample deposition or the scanning force in the tunneling junction, which either prevent from the electrons tunneling through or produce low resolution images. The reason for this formation tendency is not clear yet; probably the interaction among the backbones of the molecule is much stronger than that between the backbones and the substrates. Since in principle STM requires conductive surfaces for the electrons to tunneling through the barrier, DNA molecules may be too well insulated to permit the tunneling (compared to organic film such as $C_4$ SAM). If a method could be found to maintain the DNA molecules in their extended form on the substrate, the successful molecular imaging will be much closer to a realizable technology. It is also probable that AFM methods would be better-suited to the development of deposition techniques, since AFM is unaffected by thick and insulating films.

## Conclusion

This work has used ex-situ in-air STM to examine (1) butanethiol monolayers (2) butanethiol sub-monolayer formations and (3) DNA adsorbates onto high-quality graphite and gold surfaces, along with the controlled gold substrate treatments used in these experiments. These studies are very important to the understanding the role of STM for characterizing the organic interfacial films and biological targets. Specially, we have shown:

(1) When exposed to ***S*** acid solution, the Au/mica surface appears to have been oxidized and dissolved layer by layer--- small pits, holes, "worm-like" images, images with isolated islands, then images with isolated islands and new etching pits revealing the etching cycle.

(2) The ***S*** etching rate is slower in the lower regions on the Au/mica surface. After 10 min exposure to the acid the etching becomes less effective, which is probably due to the surface oxidation.

(3) The ***P*** acid etching is more aggressive than ***S*** acid etching and much more difficult to control.

(4) The molecularly resolved superlattice structures of $C_4$/Au(111) self-assembled monolayer and sub-monolayer that have been deposited and equilibrated in solution. The monolayer films have significantly higher surface coverages than monolayers that have been allowed to equilibrate under vacuum conditions, and marginally greater coverage than films produced by extended gas-phase dosing. The surface structure reported herein is characterized by extended stripe features 10.1 Å wide and up to 50 nm in length, with internal molecular structure that is assigned to the methyl terminations of the $C_4$ chains. We have also observed variations in elevations among the stripes that have been tentatively ascribed to adsorption in the *fcc* and *hcp* sites of the Au(111) lattice.

(5) the aggregated island-like formations on the sub-monolayer films; the local structure and density of these organic islands is essentially identical to that of the complete $C_4$ SAM.

The different surface defects on those films with different coverages are also observed, and are believed to be caused by incomplete lateral diffusion process.

(6) images of different DNA adsorbates on different prepared substrates, mostly in lower resolution. The interpretation of these images is significantly more complicated.

As the representative of a new generation of microscope, the STM has the advantage of revealing structural and electrical properties at the atomic scale, along with its limitation for organic and biological systems. It can characterize the surface structures in molecular or even atomic resolution for some organic systems like $C_4$ SAMs on gold surface, but may be not very suitable for other systems like the DNA adsorbates. New DNA deposition techniques need to be developed to immobilize the fully extended individual DNA molecules on the substrates.

## Annex Instrumention

The Schematic view of the STM used in this work is illustrated in Figure A.1, which is a home-built STM operated in air. Most of the components used are compatible with vacuum so that the same design can be applied to vacuum-based STM. The scanning range can be varied from a few nanometers to several micrometers while the tunneling current can be stabilized from 30 pA - 3 nA. The scanner is a piezoelectric tube (EBL #4, 6mm × 0.5mm × 13mm, Staveley Sensors, Inc.). The tube, made from ceramic PZT-4 [$Pb(Zr,Ti)O_3$] and metalized on the outer and inner surfaces, is poled in the radial directions. The outside metal coating is split into four longitudinal sections of equal area. The two mirror-symmetric voltage driving signals $X^+/X^-$ are applied to the two diagonally opposite electrodes, and another two signals $Y^+/Y^-$ are applied to the two electrodes left, as shown in Figure A.1.

This design maximizes the orthogonality of the scanning axes. The tip is installed in the center of the scanner by an tip holder with a ceramic insulator between them. The inner metal coating is connected to instrumental ground , which helps to shield the electronic noise to the tip from the scanning voltages applied to the tube; the tip "Z" position while scanning is controlled by a voltage added to all of the outer electrodes $X^+/X^-/Y^+/Y^-$ simultaneously, which extends or shrinks the scan tube in the Z direction. This arrangement ensures that the applied field is never in the depoling direction for the piezoelectric tube. The lateral sensitivities of the scanner are ~10 nm/V in the X, Y direction, which was precisely calibrated by atomic resolution HOPG images.

The sample is fixed with a sample holder, which is a $\phi$2.5 cm × 0.6 cm piece of hardened stainless steel. The sample holder has a magnet inside to attach itself on the top of the coarse sample positioner. The sample positioner (Burleigh Instruments, Inc.) is a clamp-step device to bring the sample to the tunneling range with respect to the fixed tip. This device uses piezoelectric clamps as well as a piezoelectric body and works like an inchworm: clamping one foot to a base, expanding the body, clamping the other foot to the base while releasing the

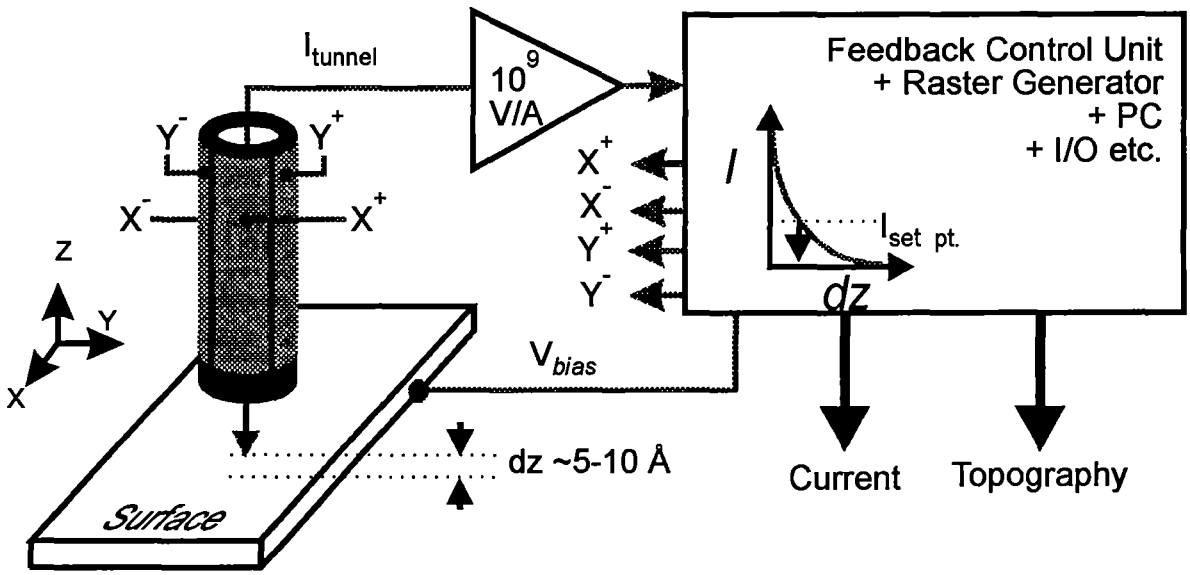


**Figure A.1** The schematic view of the STM

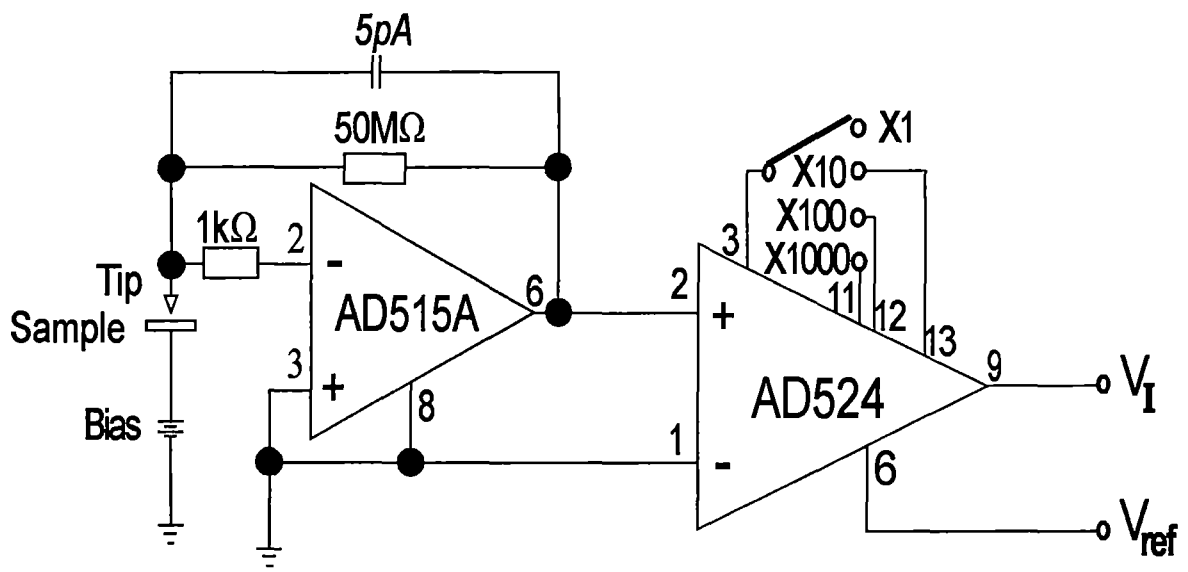


**Figure A.2** The schematic view of the preamplifier

first foot, and then contracting the body. A piece of steel is fastened to the top of the inchworm to attach the sample holder. The approach of the sample to tunneling range (~1 nm tip-sample separation) is controlled by the inchworm driver ( IWC100, RHK Technology Inc.), which can be operated manually ( coarse approach ) or automatically (precise control ). The approach starts with coarse approach manually, in which the tip-sample separation is monitored with an optical microscope. After the tip-sample separation is too small to be monitored by eyes (usually ~10-30 μm), the computer-controlled automatic approach is followed; the sample is stepped a small distance (~200 nm) towards the tip, with the tip fully retracted. After each step the tip is extended to see if any tunneling current can be detected. In this way the sample is automatically brought to within the tunneling range of the tip, minimizing the risk of crashing the tip into the sample.

As shown in Figure A.1, the preamplifier converts the tunneling current to an analog voltage and passes this signal to the feedback control unit. A bias potential (typically 0.1~1.0 V) can be applied to the sample, either positively or negatively. The current is measured at the tip, which is kept at the virtual ground. The amplifier is built around an operational amplifier AD515AL (Figure A.2), which has a low bias current ( maximum 0.075 pA ) and high input impedance ( up to $10^{11}\Omega$ ). The gain of this stage is $5\times10^{7}$ V/A. With the precision instrumentation amplifier AD524, four output gains, from 1 to 1000, are set up by a switch in the board so that the preamplifier gain can be varied from $5\times10^{7}$ V/A to $5\times10^{10}$ V/A. It offers the advantage of being able to operate the STM across a wide range of the tunneling currents for different applications. Under the present conditions, the STM could be successfully operated at the first two gain sets, where the tunneling current set is varied from 30 pA to 3 nA. If the noise level (such as electronic, acoustic, and vibrational noises) can be further diminished, the current may be stabilized at even lower setpoints. Special care is taken in the design of the preamplifier to limit the electrostatic coupling because of the high impedance of the tunneling junction.

The vibration isolation system in this STM consists a stack of metal plates with viton damper between each pair of the plates. There are six layers in total, where lower four are

made from aluminum and top two from brass. The STM head, in which the scanner, preamplifier and sample positioner are constructed together with a piece of InVar, is fixed on the topmost brass plate. All of these parts are contained within a Faraday cage with foam layers to shield the microscope from electrical and acoustic noises. The electronic signals are connected with BNC cables to the connectors inside the STM box. After the connectors, the thin cable wires ($\phi$=0.16 mm, Belden) are used to introduce these signals to the inchworm and the preamplifier. These wires are fixed to the stacked plates three times to avoid introducing electronic noises to the microscope head by vibrational coupling.

In principle, the eigen-frequencies of stacked metal plates vibration isolation system are higher (usually 10-100 Hz) than the environmental vibrations because of the stiffness of the viton and the limited compressible length. Though the eigen-frequency reduces as the number of stacked plates increases, it is impractical to achieve a resonant frequency below 10 Hz. An extra vibration isolation support was added to further damp low frequency vibrations. It is an optical table ( Model 5104-3648, Kinetic Systems Inc.) floating on compressed air. The resonant frequency of this table is 1Hz and the amplification near this frequency is small. This system works very well and a number of STM images in high quality have been acquired. But following the transfer of the lab during this work, the acoustic noise of the new site, mainly at 56 Hz, had deleterious impact on the stability of the tunneling junction. Rather than attempting further shield the microscope, the STM was transferred to a smaller, quieter room. Unfortunately, the room is too small for the optical table so that a new isolation stage has been applied. This new arrangement has a suspension stage of the whole STM system which is fixed on a heavy plate. Four viton (13cm×14cm×6mm ) O-rings are used for this suspension. The resonant frequency was not measured but the STM experiments confirm that the vibration can be attenuated effectively.

Since the STM is operated in air, any change of the ambient environment may affect its performance, especially the moisture. We have found that the leakage current could increase into nano-ampere regime when the humidity of the environment increases. This leaking current is probably due to a weakly conductive water layer formed between the tip (where the

current is measured) and the piezo elements of the scan tube, where the high voltages are applied. "Drierite" is used in the STM box to dehumidify the air in the box, which significantly decreased the leakage current. The Drierite was replaced immediately when its color tranformed from blue to purple.

The scanning and data acquisition are controlled by a PC compatible computer with three boards : (1) a digital AT-AO-6/10 board and a AT-MIO-16F-5 board from the National Instruments, (2) a STM control board from ABLE Signal Company, designed by the Lagally group of University of Wisconsin. The scan parameters, e.g., scan size, sample bias, gains, etc., are easily adjusted by computer control. The software protocol developed in this lab for STM is composed of all the functions needed in experiment, e.g., automatic sample approach, image scanning, image processing.

The lateral sensitivities of the scanner are calibrated by atomically resolved STM images of HOPG surfaces, and the vertical coordinates calibrated by the 2.36Å single atomic step heights of the freshly prepared Au/mica films. The uncertainty of the lateral calibration on small scan areas is 1-5%, and is due principally to non-orthogonalities of the XY electrodes of the scan tube.

## References


1. B. Alberts, D. Bray, J. Lewis, M. Raff, K. Roberts, J. D. Watson, *Molecular Biology of the Cell,* 2nd Ed., Garland Publishing Inc., New York & London, **1989**.
2. M. J. Allen, R. J. Tench, J. A. Mazrimas, M. Balooch, W. J. Siekhaus, R. Balhorn, *J. Vac. Sci. Technol.*, **1991**, *B9*, 1272.
3. D. P. Allison, J. R. Thompson, K. B. Jacobson, R. J. Warmack, T. L. Ferrell, *Scanning Microscopy* **1990**, *4*, 517.
4. D. P. Allison, L. A. Bottomley, T. Thundat, G. M. Brown, R. P. Woychik, J. J. Schrick, K. B. Jacobson, R. J. Warmack, *Proc. Natl. Acad. Sci. USA,* **1992**, *89*, 10129.
5. C. A. Alves, E. L. Smith, M. D. Porter, *J. Amer. Chem. Soc.* **1992**, *114*, 1222.
6. C. D. Bain, E. B. Troughton, Y. -T. Tao, J. Evall, G. M. Whitesides, R. G. Nuzzo, *J. Amer. Chem. Soc.* **1989**, *111*, 321.
7. J. V. Barth, H. Burne, G. Ertl, R. J. Behm, *Phys. Rev. B* **1990**, *42*, 9307.
8. F. Bensebaa, T. H. Ellis, A. Badia, R. B. Lennox, *J. Vac. Sci. Techn. A* **1995**, *13*, 1331.
9. T. P. Beebe Jr., T. E. Wilson, D. F. Ogletree, J. E. Katz, R. Balhorn, M. B. Salmeron, W. J. Siekhaus, *Science* **1989**, *243*, 370.
10. L. A. Bottomley, J. N. Haseltine, D. P. Allison, R. J. Warmack, T. Thundat, R. A. Sachleben, G. M. Brown, R. P. Woychik, K. B. Jacobson, T. L. Ferrell, *J. Vac. Sci. Technol.* **1992**, *A10*, 591.
11. J. P. Bucher, L. Santesson, K. Kern, *Langmuir* **1994**, *10*, 979.
12. S. Buchholz, J. P. Rabe, *Angew. chem. Int. Ed. Engl.* **1992**, *31*, 189.
13. C. Bustamante, D. Keller, *Physics Today* Dec. **1995**, 32.
14. N. III Camillone, C. E. D. Chidsey, G. -Y. Liu, G. Scoles, *J. Chem. Phys.* **1993**, *98*, 3503.
15. N. III Camillone, P. Eisenberger, T. Y. B. Leung, P. Schwartz, G. Scoles, G. E. Poirier, M. J. Tarlov, *J. Chem. Phys.* **1994**, *101*, 11031.

16. C. J. Chen, *J. Vac. Sci. Technol.* A **6**, 319 (1988); and *Phys. Rev. Lett.* **1990**, *65*, 448.

17. C. E. D. Chidsey, D. N. Loiacono, T. sleator, S. Nakahara, *Surf. Sci.* **1988**, *200*, 45.

18. C. E. D. Chidsey, G. -Y. Liu, P. Rowntree, G. Scoles, *J. Chem. Phys.* **1989**, *91*, 4421.

19. C. Clemmer, T. P. Beebe, *Science* **1991**, *251*, 640.

20. A. Cricenti, S. Selci, G. Chiarotti, F. Amaldi, *J. Vac. Sci. Technol.*, **1991**, *B9*, 1285.

21. E. Delamarche, B. Michel, Ch. Gerber, D. Anselmetti, H. -J. Güntherodt, H. Wolf, H. Ringsdorf, *Langmuir* **1994**, *10*, 2869.

22. J. A. DeRose, T. Thundat, L. A. Nagahara, S. M. Lindsay, *Surf. Sci.* **1991**, *256*, 102.

23. J. A. DeRose, S. M. Lindsay, L. A. Nagahara, P. I. Oden, T. Thundat, R. L. Rill, *J. Vac. Sci. Technol.* **1991**, *B9*, 1166.

24. L. H. Dubois, R. G. Nuzzo, *Annu. Rev. Phys. Chem.* **1992**, *43*, 437.

25. L. H. Dubois, B. R. Zegarski, R. G. Nuzzo, *J. Chem. Phys.* **1993**, *98*, 678.

26. D. M. Eigler, P. S. Weiss, E. K. Schweizer, N. D. Lang, *Phys. Rev. Lett.* **1991**, *66*, 1189.

27. P. Fenter, A. Eberhardt, P. Eisenberger, *Science* **1994**, *266*, 1216.

28. A. J. Fisher, P. E. Blöchl, *Phys. Rev. Lett.* **1993**, *70*, 3263.

29. P. K. Hansma, V. B. Elings, O. Marti, C. E. Bracker, *Science* **1988**, *242*, 209.

30. U. Harten, A. M. Lahee, J. P. Toennies, Ch. Wöll, *Phys. Rev. Lett.* **1985**, *54*, 2619.

31. Y. Hasegawa, Ph. Avouris, *Science* **1992**, *258*, 1763.

32. M. Hegner, P. Wagner, G. Semenza, *Surf. Sci.* **1993**, *291*, 39.

33. M. Hegner, P. Wagner, G. Semenza, *FEBS Letters* **1993**, *336*, 452.

34. E. Holland-Moritz, J. Gordon II, G. Borges, R. Sonnenfeld, *Langmuir* **1991**, *7*, 301.

35. H. Honbo, S. Sugawara, K. Itaya, *Anal. Chem.* **1990**, *62*, 2424.

36. J. Hu, M. Wang, H.-U. G. Weier, P. Frantz, W. Kolbe, D. F. Ogletree, M. Salmeron, *Langmuir* **1996**, *12*, 1697.

37. T. W. Jing, A. M. Jeffrey, J. A. DeRose, Y. L. Lyubchenko, L. S. Shlyakhtenko, R. E. Harrington, E. Appella, J. Larsen, A. Vaught, D. Rekesh, F.-X. Lu, S. M. Lindsay, *Proc. Natl. Acad. Sci. USA* **1993**, *90*, 8934.

38. J. Kang, P. A. Rowntree, *Langmuir* **1996**, *12*, 2813.

39. J. Kang, P. A. Rowntree, *submitted for publication.*

40. J. Kang, K. D. Truong, P. A. Rowntree, *submitted for publication.*

41. D. S. Karpovich, G. J. Blanchard, *Langmuir* **1994**, *10*, 3315.

42. Y.-T. Kim, R. L. McCarley, A. J. Bard, *J. Phys. Chem.* **1992**, *96*, 7416.

43. N. D. Lang, *Phys. Rev. Lett.* **1987**, *58*, 45.

44. Y. Li, J. Huang, R. T. Jr McIver, , J. C. Hemminger, *J. Amer. Chem. Soc.* **1992**, *114*, 2428.

45. S. M. Lindsay, O. F. Sankey, Y. Li, C. Herbst, A. Rupprecht, *J. Phys. Chem.* **1990**, *94*, 4655.

46. S. M. Lindsay, N. J. Tao, J. A. DeRose, P. I. Oden, Y. L. Lyubchenko, R. E. Harrington, L. Shlyakhtenko, *BioPhys. J.* **1992**, *61*, 1570.

47. R. L. McCarley, A. J. Bard, *J. Phys. Chem.* **1992**, *96*, 7410.

48. R. L. McCarley, D. J. Dunaway, R. J. Willicut, *Langmuir* **1993**, *9*, 2775.

49. O. Marti, M. Amrein, *STM and SFM in Biology*, Academic Press Inc., **1993**.

50. C. A. McDermott, M. T. McDermott, J.-B. Green, M. D. Porter, *J. Phys. Chem.* **1995**, *99*, 13257.

51. G. C. McGonigal, R. H. Bernhardt, D. J. Thomson, *Appl. Phys. Lett.* **1990**, *57*, 28.

52. G. C. McGonigal, R. H. Bernhardt, Y. H. Yeo, D. J. Thomson, *J. Vac. Sci. Technol.* **1991**, *B9*, 1107.

53. W. Mizutani, M. Shigeno, M. Ono, K. Kajimura, *Appl. Phys. Lett.* **1990**, *56*, 1974.

54. V. N. Morozov, N. C. Seeman, N. R. Kallenbach, *Scanning Microscopy* **1993**, *7*, 757.

55. H. Nejoh, *Appl. Phys. Lett.* **1990**, *57*, 2907.

56. W. Pan, C. J. Durning, N. J. Turro, *Langmuir* **1996**, *12*, 4469.

57. G. E. Poirier, M. J. Tarlov, *Langmuir* **1994**, *10*, 2853.

58. G. E. Poirier, M. J. Tarlov, Rushmeier, H. E., *Langmuir* **1994**, *10*, 3383.

59. G. E. Poirier, M. J. Tarlov, *J. Phys. Chem.* **1995**, *99*, 10966.

60. M. D. Porter, T. B. Bright, D. L. Allara, C. E. D. Chidsey, *J. Amer. Chem. Soc.* **1987**, *109*, 3559.

61. C. E. Rabke-Clemmer, A. J. Leavitt, T. P. Beebe Jr., *Langmuir* **1994**, *10*, 1796.

62. K. Reichelt, H. O. Lutz, *J. Crystal Growth* **1971**, *10*, 103.

63. W. Saenger, *Principles of Nucleic Acid Structure*, Springer-Verlag New York Inc., **1984.**

64. H. Sellers, *Surf. Sci.* **1993**, *294*, 99.

65. H. Sellers, A. Ulman, Shnidman, Y., Eilers, J. E., *J. Amer. Chem. Soc.* **1993**, *115*, 9389.

66. C. Shönenberger, J. A. M. Sondag-Huethorst, J. Jorritsma, L. G. J. Fokkink, *Langmuir* **1994,** *10*, 611.

67. C. Shönenberger, J. Jorritsma, J. A. M. Sondag-Huethorst, L. G. J. Fokkink, *J. Phys. Chem.* **1995**, *99*, 3259.

68. J. K. Spong, H. A. Mizes, L. J. LaComb Jr, M. M. Dovek, J. E. Frommer, J. S. Foster, *Nature* **1989**, *338*, 137.

69. L. Strong, G. M. Whitesides, *Langmuir* **1988**, *4*, 546.

70. J. D. Swalen, D. L. Allara, J. D. Andrade, E. A. Chandross, S. Garoff, J. Isreaelachvili, T. J. McCarthy, R. Murray, R. F. Pease, J. F. Rabolt, K. J. Wynne, H. Yu, *Langmuir* **1987**, *3*, 932.

71. J. A. Stroscio, W. J. Kaiser, *Scanning Tunneling Microscopy*, Academic Press Inc., **1993**.

72. J. Tersoff, D. R. Hamann, *Phys. Rev.* **1985,** *B* 31, 805; and *Phys. Rev.* **1983,** *B50*, 1998.

73. J. Tersoff, *Phys. Rev.* **1990**, *B41*, 1235.

74. K. D. Truong, P. A. Rowntree, *J. Phys. Chem.*, in press.

75. A. Ulman, *Introduction to Ultrathin Organic Films from Langmuir-Blodgett to Self-Assembly,* Academic Press, San Diego, **1991.**

76. B. Venkataraman, J. J. Breen, G. W. Flynn, *J. Phys. Chem.* **1995**, *99*, 6608.

77. B. Venkataraman, G. W. Flynn, J. L. Wilbur, J. P. Folkers, G. M. Whitesides, *J. Phys. Chem.* **1995**, *99*, 8684.

78. C. M. Vitus, A. J. Davenport, *J. Electrochem. Soc.* **1994**, *141*, 1291.

79. J. D. Watson, N. H. Hopkins, J. W. Roberts, J. A. Steitz, A. M. Weiner, *Molecular biology of the Gene*, The Benjamin/Cummings Publishing Company Inc., **1987.**

80. A. Wawkuschewski, H. -J. Cantow, S. N. Magonov, *Langmuir* **1993**, *9*, 2778.

81. A. L. Weisenhorn, H. E. Gaub, H. G. Hansma, R. L. Sinsheimer, G. L. Kelderman, P. K. Hansma, *Scanning Microscopy* **1990**, *4*, 511.

82. C. A. Widrig, C. A. Alves, M. D. Porter, *J. Amer. Chem. Soc.* **1991**, *113*, 2805.